Pathogenetic mechanisms of muscle-specific ribosomes in dilated cardiomyopathy

Michael R. Murphy[1,2,#], Mythily Ganapathi[3], Teresa M. Lee[4], Joshua M. Fisher[4], Megha V. Patel[5,6], Parul Jayakar[7], Amanda Buchanan[8], Alyssa L Rippert[9,10], Rebecca C. Ahrens-Nicklas[9,11], Divya Nair[9,10], Rajesh K. Soni[12], Yue Yin[1,2,13], Feiyue Yang[1,2], Muredach P. Reilly[1], Wendy K. Chung[14], & Xuebing Wu[1,2,#]

[1]Division of Cardiology, Department of Medicine, Columbia University Irving Medical Center, New York, NY 10032, USA

[2]Department of Systems Biology, Columbia University Irving Medical Center, New York, NY 10032, USA

[3]Department of Pathology and Cell Biology, Columbia University Irving Medical Center, New York, NY 10032, USA

[4]Department of Pediatrics, Columbia University Medical Center Irving Medical Center, New York, NY 10032, USA

[5]Department of Pediatrics, Nicklaus Children's Hospital, Miami, FL 33155, USA

[6]Current: Children's Wisconsin, Medical College of Wisconsin, Milwaukee, WI 53226, USA

[7]Division of Genetics and Metabolism, Nicklaus Children's Hospital, Miami, FL 33155, USA

[8]Illumina Inc., San Diego, CA, USA

[9]Division of Human Genetics, Children's Hospital of Philadelphia, Philadelphia, PA 19104, USA

[10]Division of Cardiology, Children's Hospital of Philadelphia, Philadelphia, PA 19104, USA

[11]Department of Pediatrics, Perelman School of Medicine, University of Pennsylvania, Philadelphia, PA 19104, USA

[12]Proteomics and Macromolecular Crystallography Shared Resource, Herbert Irving Comprehensive Cancer Center, Columbia University, New York, NY 10032, USA

[13]Barnard College, Columbia University, New York, NY 10027, USA

[14]Department of Pediatrics, Boston Children's Hospital, Harvard Medical School, Boston, MA 02115, USA

[#]Correspondence to: mrm2267@cumc.columbia.edu (M.R.M); xuebing.wu@columbia.edu (X.W.)

Abstract

The heart employs a specialized ribosome in its muscle cells to translate genetic information into proteins, a fundamental adaptation with an elusive physiological role[1-3]. Its significance is underscored by the discovery of neonatal patients suffering from often fatal heart failure caused by severe dilated cardiomyopathy when both copies of the gene *RPL3L* are mutated[4-9]. RPL3L is a muscle-specific paralog[1-3] of the ubiquitous ribosomal protein L3 (RPL3), which makes the closest contact of any protein to the ribosome's RNA-based catalytic center[10]. *RPL3L*-linked heart failure represents the only known human disease associated with tissue-specific ribosomes, yet the underlying pathogenetic mechanisms remain poorly understood. Intriguingly, disease is linked to a large number of mostly missense variants in *RPL3L*, and *RPL3L*-knockout resulted in no severe heart defect in either human or mice[3, 11-13], challenging the prevailing view that autosomal recessive diseases are caused by loss-of-function mutations. Here, we report three new cases of *RPL3L*-linked severe neonatal heart failure and present a unifying pathogenetic mechanism by which a large number of variants in the muscle-specific ribosome led to disease. Specifically, affected families often carry one of two recurrent toxic gain-of-function variants alongside a family-specific putative loss-of-function variant. While the non-recurrent variants often trigger partial compensation of *RPL3* similar to *Rpl3l*-knockout mice, both recurrent variants exhibit increased affinity for the RPL3/RPL3L chaperone GRWD1[14-16] and 60S biogenesis factors, sequester 28S rRNA in the nucleus, disrupt ribosome biogenesis, and trigger severe cellular toxicity that extends beyond the loss of ribosomes. These findings provide critical insights for genetic screening and therapeutic development of neonatal heart failure. Our results suggest that gain-of-toxicity mechanisms may be more prevalent in autosomal recessive diseases, and a combination of gain-of-toxicity and loss-of-function mechanisms could underlie many diseases involving genes with paralogs.

Main

The heart is a remarkable organ, beating continuously throughout a human lifetime with a minimal need to replenish its muscle cells (cardiomyocytes)[17]. This extraordinary durability is attributed to many unique adaptations in cardiomyocytes. One of the most fundamental yet least understood adaptations is that cardiomyocytes use a specialized ribosome to decode genetic information and synthesize proteins[1-3]. Although ribosomes in all cells use the same genetic code, the composition of the ribosome itself—a delicate molecular machine comprising 80 ribosomal proteins and 4 ribosomal RNAs (rRNAs)—can differ across cell types[18-24]. The most striking variation occurs in cardiomyocytes. During vertebrate heart development, the ubiquitous core ribosomal protein L3 (RPL3)—a gatekeeper of the ribosome's decoding center[25] and the protein closest to the ribosome's RNA-based active site[10]— is gradually replaced by its paralog, RPL3-like (RPL3L)[1, 26]. RPL3L shares 74% amino acid identity with RPL3[1, 2] and eventually becomes the dominant form in adult human left ventricular cardiomyocytes (95%)[27], to a lesser extent in skeletal muscle (60%), and barely detectable in non-muscle cells[28]. Interestingly, this switch is reversed during adult muscle growth (hypertrophy) following injury or atrophy[2, 12, 29]. The physiological role of this highly conserved and tightly regulated ribosomal switching remains poorly understood, highlighting a crucial gap in our understanding of cardiac biology at the most fundamental level.

The essential role of RPL3L and the specialized ribosome in the heart is underscored by an increasing number of severe neonatal heart failure cases caused by dilated cardiomyopathy (DCM) associated with *RPL3L* mutations[4-9]. First identified by our team[4], this condition has been classified as a new subtype of DCM, Dilated Cardiomyopathy-2D (CMD2D, OMIM# 619371). It stands out as most known DCM genes encode proteins associated with the sarcomere[30-32], the contractile unit of the muscle. *RPL3L*-linked DCM was the first—and remains the only—known human disease caused by mutations in tissue-specific ribosomes. Among seven independent affected families, individuals with mutations in both *RPL3L* alleles consistently develop severe DCM, often resulting in fatal heart failure[4-9]. In contrast, heterozygous parents and siblings carrying a single mutant allele remain unaffected with the early onset DCM. While the autosomal recessive inheritance pattern suggests a loss-of-function of these variants and RPL3L deficiency as the likely cause of DCM, *Rpl3l* knockout (KO) mice generated by multiple labs display only mild cardiac dysfunction[3, 11-13]. This is unexpected given the 96% homology between human and mouse RPL3L proteins and that the highly regulated RPL3-RPL3L switch is also conserved in mice[12].

The discrepancy between early onset fatal disease in humans and mild phenotypes in mice suggests either species-specific differences in heart biology or that the DCM-causing autosomal recessive *RPL3L* mutations have effects beyond simple loss-of-function, rendering them unsuitable for modeling with KO mice. While rarely reported, autosomal recessive mutations can cause disease via toxic gain-of-function[33]. Notably, in all *Rpl3l* KO mouse models, regardless how they were generated—whether through a frameshifting deletion of the entire exon 2[3], short frameshifting deletions in exon 5[11, 12], or poly(A) insertion in exon 1[13]—there is a consistent up-regulation of the ubiquitous paralog Rpl3. This compensatory increase in Rpl3 has been proposed to explain the absence of a severe cardiac phenotype in mice, as Rpl3 is expected to largely fulfill the functional role of Rpl3l. The molecular mechanism underlying the *Rpl3* compensation remains

97 unclear. Whether a lack of *RPL3* compensation in human underlie the severe DCM symptoms
98 remains unexplored. A deeper understanding of the pathogenetic mechanism of *RPL3L*-linked
99 DCM, including whether *RPL3* compensation occurs and how to activate the compensation, may
100 inform future management and the development of new therapeutics for these patients. This is
101 significant as nearly half of all DCM cases—and two-thirds of pediatric cases—remain of unknown
102 etiology[30, 31, 34, 35]. More broadly, this lethal disease provides a rare opportunity to explore the
103 physiological roles of ribosomes, their tissue-specific functional specializations, and the
104 mechanisms by which their dysfunction contributes to human disease.

105 In this study, we present three newly identified cases of *RPL3L*-linked severe neonatal heart failure
106 and uncover a distinctive pathogenetic mechanism through integrated analyses of population
107 genetic data, patient cardiac tissue, and isogenic cells expressing *RPL3L* variants.

108 Hotspot G27D and D308N/V are potential driver mutations

109 We identified three additional unrelated cases of *RPL3L*-associated early onset CMD2D, increasing
110 the total number of affected families to ten (Supplemental Information). Similar to previously
111 reported cases[4-9], all three families are associated with compound heterozygous variants, i.e., each
112 affected individual carry two different variants on separate alleles. Interestingly, all three cases
113 share the D308N variant, a missense amino acid substitution at position 308 that changes aspartic
114 acid (D) to asparagine (N). The affected individuals co-inherit one of three additional variants: a
115 missense variant (R58Q), a truncating frameshift variant (T340Nfs*25), or a splice donor variant
116 (c.1167+1G>A) that causes skipping of exon 9 (Δexon9)[36]. The latter two variants are predicted to
117 result in loss-of-function.
118
119 The three new cases highlight three prominent features characteristic of *RPL3L*-linked DCM across
120 all reported cases: compound heterozygosity, hotspot variants, and the pairing of hotspot variants
121 with putative loss-of-function variants. First, all but one affected families exhibit compound
122 heterozygous variants in *RPL3L* (lines in **Fig. 1a**). The only exception is a homozygous R116H variant
123 identified in a consanguineous population[7]. Across ten families, at least one unique variant is
124 present per family, with a total of 14 distinct variants identified. Second, while variants are
125 distributed across nearly the entire RPL3L protein (**Fig. 1a-b**), two notable hotspots emerge: D308
126 (D308N or D308V), observed in five families, and G27 (G27D), found in three additional families
127 (**Fig. 1a**). Collectively, D308N/V and G27D account for 80% (8/10) of *RPL3L*-linked DCM families.
128 These families appear to be unrelated, as evidenced by their diverse geographic locations, with
129 the three families carrying the G27D variant residing in the United States, Spain, and China. Lastly,
130 among the eight families carrying one of the two hotspot variants, four harbor a paired frameshift
131 or splice variant (**Fig. 1a**), typically considered (partial) loss-of-function, raising the possibility that
132 the missense variants identified in the remaining four families may also result in loss of function.
133
134 Notably, the ten missense variants can be categorized into two groups based on allele frequency
135 and pathogenicity predicted by AlphaMissense[37], a state-of-the-art deep learning model built on
136 the AlphaFold2 protein structure prediction tool[38] (**Fig. 1c**). The hotspot variants G27D and
137 D308N/V fall into the group with extremely low allele frequencies in the general population (<10^{-}

138 [5], gnomAD[39]) and are predicted to be highly pathogenic. The rarity of these hotspot variants in the
139 general population argues against the hypothesis that their recurrence in patients is due to
140 increased DNA mutability. Instead, the repeated occurrence of these ultra-rare missense
141 mutations in a significant proportion of DCM families strongly challenges a loss-of-function
142 mechanism for these variants, especially considering that neither G27 nor D308 corresponds to
143 residues known to be critical for RPL3/RPL3L's role in the ribosome[10, 25]. The high-pathogenicity
144 group also includes the V231F variant, another extremely rare (~10^{-6}) variant in the population
145 and predicted to be highly pathogenic by AlphaMissense. It is possible that with more cases to be
146 discovered, V231F may also be found to be a hotspot mutation similar to G27D and D308N/V in
147 the same group. Variants in the low-pathogenicity group are more frequent (still very rare, 10^{-5} to
148 10^{-4}) and predicted to be less pathogenic (**Fig. 1c**). Interestingly, with the exception of the
149 homozygous R116H mutation, each affected individual carries one mutation from the high-
150 pathogenicity group and another mutation from the low-pathogenicity group (linked by dashed
151 lines).

152 Consistent with the absence of a severe cardiac phenotype in *Rpl3l* KO mice, live human knockouts
153 of *RPL3L* have been identified in large-scale genetic studies, including gnomAD[39], All of Us[40], and
154 UK Biobank[41] (**Fig. 1d**). One individual carries a premature stop codon at arginine 226 in both
155 alleles (R226X), truncating nearly half of the protein (full-length RPL3L is 407 amino acids), a
156 mutation almost certainly resulting in loss-of-function. Additionally, a total of 17 individuals are
157 homozygous for the same splice donor variant found in one of the DCM families (c.1167+1G>A).
158 As shown previously[36], the splice variant causes exon 9 deletion, removing a highly conserved 40-
159 amino-acid region in RPL3L (salmon in **Fig. 1b**). Although this splice donor variant is associated
160 with an increased risk of atrial fibrillation in multiple association studies[36], homozygous individuals
161 carrying this variant appear to be alive and do not exhibit severe early-onset DCM. There are also
162 nine putative knockout humans in the Regeneron Genetics Center Million Exome (RGC-ME)
163 database[42] although detailed information about these variants is not available. The lack of severe
164 cardiac dysfunction in both putative *RPL3L* KO humans and *Rpl3l* KO mice strongly suggests that
165 the missense *RPL3L* mutations identified in DCM patients are not simply loss-of-function variants.

166 In summary, our meta-analysis of *RPL3L*-linked DCM cases reveals that affected individuals
167 frequently carry a recurrent, highly pathogenic missense variant paired with either a frameshift
168 loss-of-function variant or a low-pathogenicity missense variant. Combined with the absence of
169 severe heart defects in *RPL3L*-knockout mice and humans, these findings suggest that *RPL3L*-
170 linked DCM is likely driven by a mechanism other than loss-of-function, despite its autosomal
171 recessive inheritance pattern.

172 Ribosome defects in explanted patient hearts

173 To investigate the pathogenic mechanisms of *RPL3L* mutations in DCM, we initially focused on a
174 patient carrying the hotspot D308N variant and the T189M missense variant. This patient,
175 diagnosed and treated at our center, underwent heart transplantation and is alive to date[4]. Using
176 explanted heart ventricular tissues, we extracted total RNA to perform RNA-seq and compared the
177 results to age-matched control healthy heart ventricular tissues.

178 Unexpectedly, we observed an abnormality when the total RNA was subjected to Bioanalyzer
179 electrophoresis for quality check (**Fig. 2a**). Specifically, there is a drastic reduction in the 28S rRNA
180 peak relative to the 18S peak. The 28S rRNA is the scaffold of the 60S large subunit of the ribosome.
181 RPL3L (and the paralog RPL3) is a core component of the 60S subunit and plays a vital role in both
182 28S rRNA biogenesis and pre-60S ribosome assembly via direct binding to the 28S rRNA[43]. The loss
183 of 28S rRNA indicates a defect in 28S/60S biogenesis or turnover in patient cells, presumably due
184 to the D308N/T189M mutations in *RPL3L*.

185 The RNA-seq data revealed widespread alterations in gene expression, including 1,639 significantly
186 up-regulated genes and 2,361 significantly down-regulated genes (**Fig. 2b**). Pathway analyses
187 confirmed up-regulation of gene signatures associated with systolic heart failure and apoptosis,
188 and interestingly, a massive up-regulation of genes associated with fetal cardiac myeloid cells,
189 consistent with increased inflammation in failing hearts[44] (**Fig. 2c**).

190 In line with impaired ribosome biogenesis, many ribosomal protein genes are differentially
191 expressed, with more down-regulated than up-regulated (**Fig. 2b**). *RPL3L* is down-regulated by
192 approximately two-fold, although not significantly (adjusted P = 0.6). Both D308N and T189M
193 alleles are expressed at a similar level as indicated by sequencing read coverage (**Fig. 2d**).

194 Surprisingly, unlike the robust increase of *Rpl3* mRNA and protein in *Rpl3l* KO mice, there was no
195 compensatory up-regulation of *RPL3* mRNA in the patient's heart tissue (**Fig. 2b**). Instead, *RPL3* is
196 slightly down-regulated (by 24%, adjusted P=0.66) like many other ribosomal protein genes.

197 To confirm the lack of *RPL3* compensation in the DCM heart tissue, we also examined protein
198 expression using mass spectrometry. Indeed, when normalized to the total abundance of 40S
199 ribosomal proteins, there is a significant decrease in RPL3 abundance with no change in RPL3L (**Fig.**
200 **2e**). Consistent with a 60S biogenesis defect, there is a mild but significant decrease in total 60S
201 ribosomal protein level relative to that of the 40S. Similar to the RNA-seq data (**Fig. 2d**), the D308N
202 variant is expressed at a comparable level as the T189M variant (**Fig. 2f**).

203 In the absence of compensatory RPL3 up-regulation, there will be a shortage of functional 60S
204 ribosomes in patient cells, as neither functional RPL3L nor RPL3 is present. Given the critical role
205 of ribosomes in cellular function, the loss of functional ribosomes likely contributes to
206 cardiomyocyte death and the progression of DCM. While caveats remain (see Discussion), the lack
207 of RPL3 compensation observed in human DCM patients underscores a critical divergence from
208 the *Rpl3l* KO mouse model and suggests that at least one of the two missense *RPL3L* variants
209 (D308N and T189M) are unlikely to function as simple loss-of-function variants.

210 In summary, analysis of explanted heart tissues from DCM patients demonstrates a defect in 60S
211 ribosome biogenesis and a lack of RPL3 compensation. These defects likely contribute to the loss
212 of functional ribosomes, cardiomyocyte death, and the development of heart failure in *RPL3L*-
213 linked DCM.

214 ## Hotspot variants gain toxic function to drive ribosome biogenesis defects and cellular toxicity

215 It remains unclear whether the ribosome biogenesis defect observed in explanted patient tissue
216 is caused by the hotspot D308N mutation or the accompanying T189M variant. Both variants are
217 expressed at comparable levels with no significant allele imbalance (**Fig. 2d** and **Fig. 2F**).

218 To determine the individual impact of these variants, we generated isogenic cell lines expressing
219 various RPL3L variants in the absence of RPL3 (**Fig. 3a**). These cell lines were derived from human
220 AC16 cells, ventricular cardiomyocyte-like cells commonly used to study cardiac gene expression
221 and function[45], including the regulation of ribosomes and translation in cardiac hypertrophy[46].
222 While AC16 cells do not fully recapitulate primary cardiomyocytes, our results described below
223 demonstrate their suitability for studying ribosome-related processes. Of note, *RPL3L* is not
224 expressed in iPSC-derived cardiomyocytes (iPSC-CMs) (**Extended Data Fig. 1**), consistent with the
225 notion that iPSC-CMs resemble immature fetal cardiomyocytes[47, 48], while *RPL3L* expression is
226 restricted to mature cardiomyocytes.

227 Wild-type AC16 cells naturally express only *RPL3*, not *RPL3L*. To switch to *RPL3L* variants, we first
228 introduced a doxycycline (dox)-inducible shRNA targeting *RPL3* to deplete RPL3 in an inducible
229 manner. This cell line (shRPL3-only) serves as a critical baseline control for the cellular defect and
230 toxicity caused by the loss-of-function of ribosomal proteins. Using shRPL3-only cells, we further
231 integrated a second dox-inducible transgene expressing HA-tagged *RPL3L*, either the wild type or
232 variants (**Fig. 3a**). In addition to DCM-linked *RPL3L* variants, we also included a common SNP
233 (rs34265469) predicted to result in a benign missense variant (P291L). This SNP is the most
234 common missense variant in *RPL3L*, with an allele frequency of 4.26% (TOPMed) and is
235 homozygous in at least 715 living individuals. This isogenic system enabled allele-specific switching
236 from *RPL3* to *RPL3L* at physiological level upon dox treatment (**Fig. 3b-c**).

237 Using these isogenic cell lines, we found that the loss of the 28S rRNA observed in the explanted
238 patient heart tissue (**Fig. 2a**) was faithfully recapitulated in cells expressing the D308N variant, but
239 not in those expressing the T189M variant (**Fig. 3d**). Notably, the loss of 28S rRNA in D308N cells
240 is much stronger than that of the shRPL3-only cells (**Fig. 3d**). Given that the only difference
241 between these two cell lines is the expression of the D308N variant, the stronger defect indicates
242 toxic gain-of-function of the D308N variant. Additionally, the weaker effect in the shRPL3-only cells
243 suggests that ribosome loss alone is insufficient to fully account for the defects observed in
244 patients (**Fig. 2a**).

245 Consistent with 60S ribosomal subunit biogenesis defects, sucrose gradient sedimentation
246 revealed a dramatic reduction in 60S but not 40S ribosomal subunits in D308N-expressing cells
247 compared to WT, SNP, or T189M cells (**Fig. 3e**). Accordingly, monosomes (80S) and translating
248 polysomes (poly-ribosomes), both of which contain 60S, are also depleted in D308N-expressing
249 cells (**Fig. 3e**). Notably, the loss of polysomes in D308N-expressing cells is comparable to cells not

250 expressing any *RPL3L* variant (shRPL3-only) (**Fig. 3e**), suggesting the D308N variant of RPL3L almost
251 completely blocks ribosome biogenesis.

252 In line with a severe loss of ribosomes, D308N-expressing cells exhibited a severe growth defect
253 (**Fig. 3f**, note that the y-axis is on a logarithmic scale). Expressing D308N for 10 days led to a 40-
254 fold reduction in cell counts (compared to RPL3L-WT cells, **Fig. 3f**, green vs. red). Interestingly,
255 cells expressing the D308N variant exhibit a 6.4-fold greater growth defect compared to cells
256 lacking RPL3L expression (shRPL3-only) (green vs. blue, **Fig. 3f**), again suggesting toxic gain-of-
257 function. Of note, the control cell line expressing RPL3 (shScramble) grew faster than cells
258 expressing wild type RPL3L (RPL3L-WT), mirroring a previous mouse study showing that Rpl3l
259 expression is associated with reduced protein synthesis and slower muscle cell growth[2].
260 Interestingly, cells expressing the T189M variant of *RPL3L* grew faster than cells expressing the
261 wild type *RPL3L*, which may be attributed to a higher expression of *RPL3* in this cell line (**Fig. 3b**,
262 also see below the discussion on *RPL3* compensation). The lack of deleterious effects associated
263 with the T189M variant aligns with its low pathogenicity prediction by AlphaMissense (**Fig. 1c**) and
264 is further supported by the presence of a living homozygous T189M individual in the population
265 genotyped in TOPMed. Taken together, these results indicate that the D308N variant is a toxic
266 gain-of-function variant and the primary driver of the disease in the patient carrying D308N and
267 T189M.

268 Next, we investigated the other hotspot variant G27D, together with the R161W variant found in
269 the same affected individual[4]. Similar to the D308N variant, cells expressing the G27D variant grew
270 substantially slower than those expressing the wild-type *RPL3L* (33-fold fewer cells by day 10,
271 **Extended Data Fig. 2a**), whereas cells expressing the R161W variant grew slightly faster than cells
272 expressing the WT RPL3L, similar to T189M. Consistent with a growth defect, G27D but not
273 R161W-expressing cells are depleted of 60S and 80S ribosomes as well as polysomes (**Extended**
274 **Data Fig. 2b**). These findings confirm that the hotspot variants G27D and D308N, but not their co-
275 inherited non-hotspot variants T189M and R161W, are responsible for ribosome biogenesis
276 defects and cellular toxicity.

277 ## Hotspot variants mislocalize and alter interactions with ribosome biogenesis factors

278 To further explore the molecular basis of the toxic gain-of-function of the hotspot variants, we
279 examined the subcellular localization of RPL3L variants using fluorescence imaging of the HA tag.
280 In contrast to the predominantly cytoplasmic localization of the wild-type RPL3L and the common
281 SNP variant expected from a ribosomal protein, the hotspot variants D308N and G27D both
282 exhibited nearly exclusive nuclear localization (**Fig. 4a**, green, quantified in **Fig. 4b**). Given the role
283 of RPL3/RPL3L in 60S ribosome biogenesis, this mislocalization of the hotspot variants likely disrupt
284 60S ribosome assembly. Supporting this, fluorescent probes for 28S rRNA revealed a significant
285 decrease in cytoplasmic 28S rRNA levels in D308N or G27D-expressing cells relative to the nucleus
286 (**Fig. 4a**, red, quantified in **Fig. 4c**). Notably, this 28S rRNA localization defect was not observed in
287 cells not expressing any RPL3L variant (shRPL3-only), consistent with a toxic gain-of-function of
288 both hotspot variants.

289 Intriguingly, while the non-hotspot T189M variant showed a cytoplasmic localization similar to the
290 wild type RPL3L (**Fig. 4a-b**), the other non-hotspot R161W variant, identified in the same affected
291 individual as the hotspot G27D, also mislocalizes to the nucleus (**Fig. 4a-b**). However, unlike the
292 hotspot variants and consistent with its lower predicted pathogenicity (**Fig. 1c**), R161W does not
293 cause nuclear sequestration of 28S rRNA (**Fig. 4a/c**), nor does it lead to a ribosome biogenesis
294 defect (**Extended Data Fig. 2a**) or cell toxicity (**Extended Data Fig. 2b**).

295 To gain biochemical insights into the toxicity associated with the hotspot variants, we profiled the
296 interactomes of RPL3L variants by using immunoprecipitation against HA-tag followed by mass
297 spectrometry in triplicates. Given the exclusive nuclear localization of the hotspot variants, we
298 used nuclear lysate as input for all samples. Interestingly, principal component analysis (PCA) of
299 the proteomics data separates the two hotspot variants from the rest in the first principal
300 component (PC1), suggesting dramatic rewiring of the interactome for hotspot variants (**Fig. 4d**).
301 The second principal component (PC2) separates the three nuclear variants (G27D, D308N, and
302 R161W) from the two cytoplasmic variants (T189M and WT). Interestingly, the top two proteins
303 driving the separation of hotspot variants from other variants both exhibit increased affinity for
304 the hotspot variants, supporting the concept of toxic gain-of-function effects (**Fig. 4e**). These two
305 proteins, GRWD1 and C7ORF50, although less studied in humans, have yeast homologs (Rrb1 and
306 Rbp95, respectively) that directly interact with yeast Rpl3 during 60S ribosome biogenesis. GRWD1
307 serves as the dedicated chaperone for RPL3 (and likely RPL3L as well), binding RPL3 co-
308 translationally to prevent its aggregation and degradation, ensuring its proper delivery to the
309 assembly site on nucleolar pre-60S particles[14-16]. The other protein, C7ORF50, interacts with RPL3
310 both genetically and physically, binding adjacent to RPL3 on the 28S rRNA during early pre-60S
311 ribosome biogenesis[49-51]. Several other 60S biogenesis factors, including RRP15[52], EBNA1BP2[53],
312 DDX24[54], NOP56[50], and MRTO4[55] also exhibited enrichment in the nuclear pulldown of RPL3L
313 variants (**Extended Data Fig. 3**). The sequestration of these essential 60S ribosome biogenesis
314 factors by hotspot variants likely underlies the 60S biogenesis defect and contributes to the toxic
315 gain-of-function effects associated with these variants.
316
317 In summary, our subcellular localization analysis and nuclear protein interactome profiling using
318 isogenic cell lines reveal that the hotspot variants D308N and G27D mislocalize to the nucleus,
319 leading to nuclear retention of 28S rRNA. This toxic effect is likely driven by their enhanced binding
320 to the dedicated RPL3/RPL3L chaperone GRWD1 and 60S ribosome biogenesis factors, including
321 C7ORF50.

322 ## Non-hotspot variants drive post-transcriptional *RPL3* compensatory up-regulation

323 It is intriguing that the mislocalization of the non-hotspot variant R161W to the nucleus (**Fig. 4a-**
324 **b**) did not cause ribosome biogenesis defects (**Fig. 4c** and **Extended Data Fig. 2a**) or cell toxicity
325 (**Extended Data Fig. 2b**). Western blot analysis of the polysome fractions confirmed the absence
326 of R161W from these ribosomes (**Extended Data Fig. 4**). To investigate how ribosomes can still
327 function in the absence of cytoplasmic RPL3L, we examined the expression of RPL3, which was
328 expected to be silenced by an shRNA induced alongside the R161W variant upon dox treatment
329 (**Fig. 3a**). Unexpectedly, while *RPL3* remained silenced in cells expressing most *RPL3L* variants, its

330 expression was almost fully restored in cells expressing the R161W variant, and to a lesser extent
331 in those expressing the T189M variant, at both the mRNA (**Fig. 5a**) and protein (**Fig. 5b**) levels.
332 Importantly, there was no significant change in the expression of the *RPL3*-targeting shRNA
333 (**Extended Data Fig. 5**), ruling out the possibility that *RPL3* recovery was due to loss of shRNA-
334 mediated knockdown in cells expressing R161W or T189M. These results suggest that, similar to
335 *Rpl3l*-KO mice, the expression of the non-hotspot *RPL3L* variants R161W and T189M leads to
336 compensatory up-regulation of *RPL3*, suggesting that these variants are functionally equivalent to
337 a knockout of *RPL3L*. Supporting a model in which compound heterozygotes carry a toxic hotspot
338 variant alongside a loss-of-function variant, frameshifting or splice variants were identified in four
339 of the eight families with hotspot variants (**Fig. 1a**).

340 To elucidate the mechanism behind this *RPL3* compensation, we first examined the transcriptional
341 activity at the *RPL3* promoter using chromatin immunoprecipitation (ChIP) against RNA
342 polymerase II (Pol II). No significant differences in transcriptional activity were observed between
343 cells expressing G27D and R161W (**Fig. 5c**). Additionally, qPCR measurements of nascent
344 transcription from intronic RNA showed no significant differences (**Extended Data Fig. 6**), ruling
345 out transcriptional up-regulation as the mechanism of *RPL3* compensation.

346 We then assessed the stability of *RPL3* mRNA by inhibiting global transcription with the RNA Pol II
347 inhibitor α-amanitin and measuring the decay of *RPL3* mRNA over time. Compared to cells
348 expressing the G27D variant, *RPL3* mRNA was significantly more stable in cells expressing the
349 R161W variant (**Fig. 5d**, $P < 0.05$). Consistent with a post-transcriptional mechanism, the increase
350 in steady-state *RPL3* level was primarily due to increased cytoplasmic *RPL3*, with no significant
351 change in the nuclear fraction (**Fig. 5e**).

352 In summary, unlike the two hotspot variants, G27D and D308N, which exhibit a gain-of-toxic
353 function, the non-hotspot variants R161W and T189M resemble a knockout effect, promoting
354 compensatory upregulation of *RPL3* by stabilizing its mRNA.

355 Impaired protein synthesis in engineered compound heterozygous cells

356 *RPL3L*-linked DCM patients often carry a combination of a hotspot variant and a non-hotspot
357 variant, such as the D308N/T189M and G27D/R161W pairs we have characterized. In our analysis
358 of explanted heart tissue from patients carrying the D308N/T189M variants, both variants were
359 detected at the RNA (**Fig. 2d**) and protein levels (**Fig. 2f**). Given the opposing effects of the hotspot
360 and non-hotspot variants on ribosome biogenesis and cell growth (**Fig. 3-5**), we sought to explore
361 the impact of these variants when both are present in the same cell, as is common in most DCM
362 patients.

363 To address this, we introduced the G27D variant into cells expressing the R161W variant, creating
364 a model of compound heterozygous cells that mirror those found in DCM patients. We chose
365 R161W over T189M because R161W triggers a stronger compensatory up-regulation of *RPL3* (**Fig.**
366 **5a-b**). Using a puromycin incorporation assay to measure nascent protein synthesis, we observed
367 a significant reduction in protein synthesis rates in the compound heterozygous cells compared to
368 those expressing R161W alone, though the rate was still higher than in cells expressing G27D alone

369 (**Fig. 6a-b**). This reduced protein synthesis rate aligns with the observed detrimental effects of
370 compound heterozygous *RPL3L* variants in humans.

371 Interestingly, *RPL3* compensation remained unaffected in the compound heterozygous cells
372 compared to cells expressing R161W alone (**Fig. 6c**). This suggests that the compensatory up-
373 regulation of *RPL3* is not sufficient to overcome the toxic effects of the G27D variant.

374 ## Discussion

375 In this study, we uncovered a unifying mechanism linking a large number of variants in muscle-
376 specific ribosomes to severe neonatal heart failure. Remarkably, affected families often carry one
377 of two toxic gain-of-function variants alongside a unique putative loss-of-function variant. The
378 loss-of-function variants include frameshift-induced truncated variants and missense variants
379 distributed across the protein, consistent with the overall high evolutionary conservation of RPL3L.
380 This unexpected pathogenetic mechanism—autosomal recessive mutations exerting gain-of-toxic
381 function other than merely loss-of-function effects—underlie the severe heart defects in humans
382 and may also explain the lack of phenotype in *RPL3L* KO mice and humans.

383 Our results show that the disease is primarily driven by two hotspot variants exhibiting toxic gain-
384 of-function effects on ribosome biogenesis. In rare diseases, hotspot variants are frequently
385 associated with toxic effects or dominant-negative traits[56-58]. Despite their rarity in the general
386 population, the missense variants G27D and D308N/V are present in eight of ten unrelated families
387 affected by DCM (**Fig. 1a**). Mechanistically, these RPL3L hotspot variants mislocalize to the nucleus
388 (**Fig. 4a-b**) and drastically rewire the network of 60S ribosome biogenesis factors (**Fig. 4d-e**).
389 Supporting a toxic gain-of-function model, both hotspot variants exhibit enhanced binding to the
390 dedicated RPL3/RPL3L chaperone GRWD1 and several early pre-60S biogenesis factors (**Fig. 4d-e**).
391 This aberrant interaction leads to sequestration of 28S rRNA in the nucleus (**Fig. 4a/c**), a defect
392 absent in cells expressing other variants or lacking RPL3L expression entirely, underscoring the
393 specific toxicity of the hotspot variants beyond simple loss-of-function. Expression of the hotspot
394 variants results in a marked depletion of ribosomes (**Fig. 3e**) and a severe cell growth defect (**Fig.
395 3f**), effects that extend beyond the consequences of ribosome loss alone. Future studies,
396 especially *in vivo* studies will be needed to elucidate how these molecular and cellular defects lead
397 to organ level failure.

398 Autosomal recessive mutations in Mendelian disorders are typically considered loss-of-function
399 mutations[59]. Rarely do they cause disease via gain-of-toxicity or dominant-negative mechanisms.
400 The only prior example known is the A673V missense mutation in the β-amyloid (Aβ) precursor
401 protein (APP), associated with familial Alzheimer's disease[33]. In this case, the mutant in the
402 homozygous state enhances Aβ peptide production, promoting the formation of amyloid fibrils,
403 the primary trigger of Alzheimer's disease. In heterozygous individuals, however, the coexistence
404 of wild-type and mutant Aβ peptides inhibits amyloidogenesis relative to either mutant or wild-
405 type Aβ peptide alone. This inhibition is likely due to conformational incompatibility between the
406 wild-type and mutant Aβ peptides. For *RPL3L*-linked heart failure, there are several possibilities
407 for why heterozygous members of families carrying the recurrent and toxic variant (e.g., G27D and
408 D308N/V) have not developed severe disease. The presence of the wild type RPL3L protein will

409 likely reduce the toxicity and result in incomplete penetrance or much delayed onset of the disease.
410 Given that yeast Rpl3 aggregates when over-expressed[14], one plausible mitigation mechanism is
411 that these RPL3L hotspot variants promote aggregation similar to the A673V Aβ variant, with wild-
412 type RPL3L in heterozygous cells preventing such aggregation and mitigating the pathogenic
413 effects.

414 Compensation by the paralog RPL3, triggered by RPL3L loss-of-function, likely explains why severe
415 disease arises only from a combined gain-of-toxicity and loss-of-function mechanism, rather than
416 loss-of-function alone. Given that 80% Mendelian disease genes have duplicated paralogs[60],
417 similar combinatorial mechanisms may be more widespread. Genetic compensation by paralogs
418 is well-documented, although the underlying molecular mechanisms often remain unclear[61-63].
419 The increased expression of *Rpl3* observed in *Rpl3l* KO mice has been proposed to explain the
420 absence of severe cardiac phenotypes in these animals, but the molecular basis of this
421 compensation is not yet understood. In this study, we demonstrate that non-hotspot missense
422 mutations, such as R161W, also up-regulate *RPL3* expression in human cells. This up-regulation
423 occurs through stabilization of cytoplasmic *RPL3* mRNA without transcriptional activation.
424 However, the *RPL3* compensation induced by the R161W variant does not fully counteract the
425 toxic effects of the G27D variant when co-expressed in human cells. These findings suggest that
426 enhancing *RPL3* compensation alone may be insufficient as a therapeutic strategy for patients
427 carrying toxic *RPL3L* mutations.

428 We observed no significant *RPL3* compensation in failing hearts explanted from human DCM
429 patients carrying the compound heterozygous RPL3L variants, D308N and T189M. This finding
430 stands in stark contrast to the robust up-regulation of *Rpl3* observed in *Rpl3l* KO mice. The absence
431 of *RPL3* compensation in humans may contribute to the disease pathology and potentially explain
432 the phenotypic differences between humans and mice. Alternatively, it could result from muscle
433 remodeling and other pathological changes in failing hearts, given that the RPL3/RPL3L switch is
434 regulated by muscle hypertrophy. Supporting the latter hypothesis that the absence of *RPL3*
435 compensation is a consequence rather than a cause of the disease, *RPL3* is down-regulated in non-
436 *RPL3L*-linked DCM[64]. Consistent with this model, *RPL3* compensation was robustly induced *in vitro*
437 in AC16 cells co-expressing same variants (D308N/T189M) found in patient cells. These findings
438 suggest that *RPL3* compensation may occur during the early stages of the disease but diminishes
439 as the condition progresses. The disease can progress even in the presence of *RPL3* compensation,
440 as shown *in vitro* that the D308N variant causes protein synthesis defect even in the presence of
441 *RPL3* compensation (**Fig. 6**). As the disease advances, the loss of *RPL3* compensation could result
442 from the complex remodeling processes in failing hearts. Future studies, including mouse knock-
443 in models that faithfully recapitulate human disease phenotypes, will be critical for testing these
444 models and uncovering the underlying mechanisms.

445 In conclusion, our systematic genetic and functional analyses shed light on the pathogenesis of
446 heart failure caused by mutations in muscle-specific ribosomes, revealing a novel mechanism
447 driven by the gain-of-toxic effects of recessive mutations. These findings provide a foundation for
448 exploring other RPL3L variants and developing targeted therapies. Notably, our results suggest
449 that gain-of-toxicity mechanisms may be more prevalent in autosomal recessive diseases than

450 previously recognized. Furthermore, the interplay between gain-of-toxicity and loss-of-function
451 mechanisms may represent a common feature in diseases involving genes with paralogs. Finally,
452 our study highlights unexpected tissue-specific pathology in otherwise universal cellular processes
453 and underscores the importance of unbiased approaches in identifying disease candidates for
454 accurate diagnosis.

455

456 ## Acknowledgments

457 We thank members of the Wu lab and the Cardiometabolic Genomics Program for discussion and
458 comments on the manuscript. This work is supported by NIH/NHLBI grant 1R01HL171664-01 and
459 Pershing Square Foundation MIND Prize (X.W.) and a postdoctoral fellowship from American Heart
460 Association (M.R.M). This research was funded in part through the NIH/NCI Cancer Center Support
461 Grant P30CA013696 and used the Genomics and High Throughput Screening Shared Resource and
462 CCTI Flow Cytometry Core. The CCTI Flow Cytometry Core is supported in part by the Office of the
463 Director, National Institutes of Health under awards S10OD030282 and S10OD020056.

464

465 ## Author contributions

466 X.W. and M.R.M. conceived the functional study and wrote the manuscript with input from all
467 authors. M.R.M. performed the majority of experiments. M.G. coordinated case reports sample
468 collection and provided critical feedback. T.M.L. and J.M.F. identified and characterized the
469 D308N/T340Nfs*26 case. M.V.P., A.B., and P.J. identified and characterized the D308N/R58Q case.
470 A.L.R., R.C.A., and D.N. identified and characterized the D308N/c.1167+1G>A case. R.K.S.
471 generated the proteomics data. Y.Y. assisted in imaging. W.K.C. contributed the D308N/T189M
472 tissue sample. W.K.C., M.P.R., and F.Y. edited the manuscript and provided critical feedback.

473

474 ## Declaration of interests

475 X.W. is a member of the Scientific Advisory Board for Epitor Therapeutics. W.K.C. serves on the
476 Board of Directors at Prime Medicine.

477

478 ## Data availability

479 RNA-seq data has been deposited in GEO. It will be released after publication.
480

481 ## Code availability

482 Data analyses were performed using publicly available software.

483

484 ## Materials and Methods

485 ### Cell Culture, Drugs and Transfection

486 AC16 cells were cultured at 37°C, 5% CO_2 in low-glucose DMEM (Fisher; 11-885-084)
487 supplemented with 10% FBS. HEK293T cells were cultured in DMEM with 10% FBS. For
488 immunofluorescence assays, 2 x 10^5 cells were plated in 6 well plates and incubated for 24 hours.
489 For stable cell generation, EZ-Tet-RPL3-shRNA was co-transfected with CMV-dR8.91 and MD2.G
490 plasmids for 72 hours in HEK293T cells to produce virus. The media was centrifuged for 5 minutes
491 at RT, filtered using 0.45µm Syringe Filter Unit (Fisher), and 200µl viral media was added to 2 x 10^5
492 AC16 cells for 48 hours prior to selection using 200µg/ml Hygromycin B until control cells (non-
493 transduced) were dead. For stable generation of pLenti-RPL3L, procedure was followed as above
494 except transduction was carried out on EZ-Tet-RPL3-shRNA/AC16 cells and selection was carried
495 out by sorting for BV421-positive cells. For mRNA stability assay, AC16 cells were treated with
496 50mg/ml a-amanitin for the indicated time points.
497

498 ### Plasmids

499 To generate plasmid expressing shRNA against RPL3, a reported high efficiency shRNA sequence
500 for RPL3 was identified (Sigma) and ~70nt single stranded oligos were ordered from IDT and
501 annealed by heating to 95°C and cooled at a rate of 5°C min^{-1}. Double-stranded oligos had two 5'
502 overhangs corresponding to NheI and EcoRI sites, respectively. dsDNA oligos were ligated to EZ-
503 Tet-pLKO-Hygro (Addgene; 85972) using Quick Ligation Kit (NEB), producing Tet-inducible RPL3
504 shRNA vector. The pLenti-RPL3L plasmid was derived from pLentiRNACRISPR_007 (Addgene;
505 138149). A gene fragment containing the wild-type human RPL3L sequence with a C-terminal HA
506 tag was delivered on pUC57 (Genewiz). PCR products for wild-type RPL3L-HA derived from pUC57,
507 the pLentiRNACRISPR_007 backbone, and EBFP (unpublished in-house plasmid) with overlapping
508 ends were assembled via Gibson cloning using NEBuilder HiFi DNA Assembly Master Mix (NEB),
509 producing Dox-inducible RPL3L and constitutive EBFP expression. To obtain RPL3L mutation
510 plasmids, primers (Supplementary Table) were designed against pUC57-RPL3L-HA with single
511 nucleotide substitutions in the 5' region of the forward primer sequence. Mutagenesis was
512 performed using Site Directed Mutagenesis Kit (NEB) as per the manufacturer's instructions.
513 pLenti-RPL3L mutations were derived similarly to the wild-type as above.
514

515 ### Immunofluorescence and FISH

516 15,000 cells were seeded on Lab-Tek II (Thermo) chamber slides and grown overnight. Cells were
517 washed once with PBS and fixed in 300µl PFA at room temperature for 15 minutes. Fixed wells
518 were washed 3x with PBS for 3 minutes, permeabilized in 0.5% Triton X-100 in PBS for 15 minutes,
519 washed 3x, and incubated in 3% BSA in PBS for 1 hour to block. Cells were then incubated in 3%
520 BSA containing primary antibody overnight at 4°C, washed 3x in PBS, then incubated for 1 hour at

521 room temperature in secondary antibody protected from light. After washing 3x, cells were
522 incubated in 1:1000 DAPI solution for 5 minutes, washed 3x, then imaged using a Nikon Eclipse Ti
523 Series confocal microscope equipped with 60x lens performed at Columbia University's Confocal
524 and Specialized Microscopy Core. RPL3L was detected using anti-HA (Thermo; 2-2.2.14).
525 Secondary staining was accomplished using goat anti-rabbit IgG (H+L) Alexa Fluor 488 (Invitrogen)
526 and goat anti-mouse IgG (H+L) Alexa Fluor 594 (Invitrogen). For rRNA FISH, cells were fixed as
527 above but permeabilized with 70% ethanol for at least 1 hr. Custom designed 28S rRNA FISH
528 probes (Supplementary Table) were designed conjugated to CAL Fluor® Red 590 dye (Stellaris) and
529 incubated with fixed samples for 16 hours in the dark. After washing using wash buffers A + B
530 (Stellaris), samples were incubated with primary anti-HA antibody as above.
531
532 Polysome fractionation
533 Sucrose gradient density ultracentrifugation was used to separate the monosomal and polysomal
534 ribosomal fractions. For human cell experiments, AC16 cells were grown in 15cm dish were lysed
535 by adding 800µl of ice-cold lysis buffer (20mM HEPES, 150mM KCl, 10mM $MgCl_2$), plus 0.5% NP-
536 40, 1x EDTA-free Protease Inhibitor Cocktail (PIC; Roche)), 2.5mM DTT, 25 U ml^{-1} Turbo DNase I
537 (Invitrogen)), 10U SuperaseIN (Thermo), 2mM Vanadyl Ribonucleoside Complex (NEB) and
538 100ug/ml CHX (Sigma) directly to the plate and scraping. Lysed material was transferred to 1.5ml
539 centrifuge tube then triturated 10x with 23-gauge syringe. Samples were incubated in 4ºC for 30
540 minutes with rotation to complete lysis, then centrifuged at 14,000g for 7 minutes. Supernatant
541 was transferred to new tube and 700ul of lysate was loaded onto a 10-50% sucrose gradient,
542 before ultracentrifugation at 38,000rpm for 2 hours. The sucrose gradient was made by combining
543 10% and 50% sucrose solutions in lysis buffer, plus 2.5mM DTT, 160U SuperaseIN, and 100µg/ml
544 CHX. Both gradient formation and fractionation was performed on a Biocomp Gradient Profiler
545 (Biocomp). For protein extraction post-fractionation, 1 volume of TCA to 4 volumes of protein
546 sample was added, incubated for 10 minutes on ice, then span at 14,000rpm for 5 minutes at 4°C.
547 Pellet was washed twice with ice-cold acetone and dried at 95°C for 5 minutes. For SDS-PAGE, 4x
548 Sample reducing agent (GenScript) diluted 1:1 in RIPA was added to dry pellet and heated for an
549 additional 5 minutes at 95°C.
550
551 Western blotting
552 Western blot analysis was performed after SDS-PAGE using standard protocols. The antibodies
553 used were anti-HA (Thermo; 2-2.2.14), anti-RPL3 (Sigma; 3365), anti-RPL28 (Invitrogen; 62192),
554 anti-RPS3 (Thermo; 2G7H4), anti-GAPDH (Invitrogen; PA1988), and anti-Vinculin (CST; E1E9V).
555
556 RNA extraction/analysis and qPCR
557 Total RNA was isolated using NucleoSpin RNA Plus kit (Macharey-Nagel) including use of gDNA
558 removal column. For rRNA analysis, 500ng RNA was ran on 2100 Bioanalyzer (Agilent) at the
559 Columbia University's Molecular Pathology Core. For qPCR, cDNA synthesis was performed using
560 500ng RNA with the SuperScript IV Reverse Transcriptase (Invitrogen) as per the manufacturers
561 protocol with oligo(dT) primers. Real-time PCR was carried out using PowerUp SYBR Green Master
562 Mix using 1:3 diluted cDNA. For qRT-PCR, triplicates were performed with 0.5µM primer and 1µl
563 cDNA per reaction in the QuantStudio 7 Flex Real-Time PCR System. Ct values obtained were
564 plotted using GAPDH mRNA as loading control. Quantifications were performed as per the MIQE

565 guidelines. Statistical tests were performed with Prism 9 and two-sided Student's t-test were used
566 to calculate the *P* values. Data are expressed as mean ± s.d. for the number of replicates indicated,
567 with $P < 0.01$ considered significant. All primer sequences are displayed in Supplementary Table.

568 Nuclear/Cytoplasmic RNA Extraction Protocol

569 Cells were washed with ice-cold PBS, scraped into 1.7ml tubes, and pelleted at 500 g for 5 minutes
570 at 4°C. Cytoplasmic RNA was extracted by lysing cells in Cytoplasmic Lysis Buffer (40 mM HEPES-
571 NaOH pH 7.5, 160 mM KCl, 10 mM $MgCl_2$, 0.5% NP-40, 0.5% glycerol, and SuperaseIn) for 30
572 minutes at 4°C with rotation, followed by centrifugation at 2000 g for 2 minutes to separate the
573 cytoplasmic supernatant. Nuclear pellets were washed in Cytoplasmic Lysis Buffer (without
574 detergent), centrifuged at 500 g for 5 minutes, and subjected to a wash with Nuclear Lysis Buffer
575 (10 mM Tris-HCl pH 8.0, 1.5 mM KCl, 2.5 mM $MgCl_2$, 5% glycerol, 0.5% Triton X-100, 0.5%
576 deoxycholate, and 20U SuperaseIN) for 15 minutes at 4°C. Final washes were performed with
577 Cytoplasmic Lysis Buffer (without detergent), and nuclei were pelleted at 2000 g for 2 minutes.
578 Both cytoplasmic and nuclear RNA were extracted as above.

579 Co-immunoprecipitation
580 To prepare magnetic bead-antibody complex, 50µl of Dynabeads Protein G (Invitrogen) was
581 washed 3x with lysis buffer then incubated with 5µl anti-HA (Thermo; 2-2.2.14) in 400µl lysis buffer
582 for 1 hour at RT with constant rotation. Magnetic bead-antibody complex was captured using
583 Magnetic Separation Rack (NEB), washed 2x with cytoplasmic lysis buffer (20mM Tris-HCl, pH 7.5,
584 150mM KCl, 10% glycerol and 0.1% NP-40) then 3x with lysis buffer. 2x 15cm plates at 80%
585 confluency were grown, cells were washed twice in ice-cold PBS and 400µl of ice-cold lysis buffer
586 was dripped onto the plate and scraped, incubated in microcentrifuged tubes after triturating 10x
587 with 23-gauge syringe, and centrifuged at 14,000g for 7 minutes. The supernatant was added to
588 bead-antibody complex and incubated with rotation at 4°C overnight. Next day, bead-antibody-
589 antigen complex was washed 3x for 10 minutes at 4°C with ice-cold lysis buffer. Protein was eluted
590 by incubation with 40µl pH 3 glycine and heating at 70°C with shaking for 10 minutes, then
591 neutralized with 1/10 volume pH 8.0 Tris.
592
593 Proteomics
594 Explanted frozen patient tissue was homogenized with pestle and mortar under liquid nitrogen
595 and lysed in RIPA for mass spectrometric analysis by the Proteomics core facility at Columbia. For
596 the global quantitative proteomic analysis, diaPASEF-based proteomics[65] was employed. Briefly,
597 frozen patient tissue samples were lysed in freshly prepared SDC lysis buffer (1% sodium
598 deoxycholate and 100 mM Tris-HCl, pH 8.5) and heated at 60°C with shaking at 1200 rpm for 15
599 minutes[66]. Protein reduction and alkylation of cysteine residues were carried out using 10 mM
600 tris(2-carboxyethyl)phosphine (TCEP) and 40 mM chloroacetamide (CAA) at 45°C for 15 minutes,
601 with shaking at 1200 rpm. The samples were then sonicated in a water bath and allowed to cool
602 to room temperature. Proteins were digested overnight with a Lys-C/trypsin mix at a 1:50 ratio
603 (µg enzyme to µg protein) at 37°C with shaking at 1400 rpm. The resulting peptides were acidified
604 with 1% trifluoroacetic acid (TFA), vortexed, and subjected to StageTip cleanup using SDB-RPS[66].
605 Peptides were then dried in a speed vacuum concentrator. Dried peptides were resuspended in

606 10 µL of LC buffer (3% acetonitrile, 0.1% formic acid), and their concentrations were determined
607 using a NanoDrop spectrophotometer. For diaPASEF analysis on the timsTOF Pro instrument, 200
608 ng of peptides from each sample were used. For liquid chromatography with tandem mass
609 spectrometry (LC-MS/MS), peptides were separated within 87 min at a flow rate of 300 nl/min on
610 a reversed-phase C18 column with an integrated CaptiveSpray Emitter (25 cm x 75µm, 1.6 µm,
611 IonOpticks). Mobile phases A and B were with 0.1% formic acid in water and 0.1% formic acid in
612 ACN. The fraction of B was linearly increased from 2 to 23% within 70 min, followed by an increase
613 to 35% within 10 min and a further increase to 80% before re-equilibration. The timsTOF Pro was
614 operated in diaPASEF mode and data was acquired at defined 32 × 50 Th isolation windows from
615 m/z 400 to 1,200. To adapt the MS1 cycle time in diaPASEF, set the repetitions to 2 in the 16-scan
616 diaPASEF scheme. The collision energy was ramped linearly as a function of the mobility from 59
617 eV at 1/K0=1.6 Vs cm^{-2} to 20 eV at 1/K0=0.6 Vs cm^{-2}. The acquired diaPASEF raw files were
618 searched using the UniProtKB/Swiss-Prot mouse database was performed using library-free
619 workflow in the DIA-NN[67] search engine, employing the default settings of the library-free search
620 algorithm with match-between-runs (MBR) enabled. A maximum of 1 trypsin missed cleavage was
621 allowed and the maximum variable modification was set to 1. Carbamidomethylation was set as
622 the fixed modification, whereas protein N-terminal methionine excision, methionine oxidation,
623 and N-terminal acetylation were set as variable modifications. The peptide length range was set
624 to 7–30 amino acids, precursor charge range 1–4, precursor m/z range 300–1800, and fragment
625 ion m/z range 200–1800. The false discovery rates (FDRs) at the protein and peptide levels were
626 set to 1%, and MS1 and MS2 mass tolerances were automatically determined by DIA-NN. Results
627 obtained from DIA-NN were subjected to further statistical analyses. Custom fasta files containing
628 mutant D308N peptides were analyzed on MaxQuant for peptide abundance relative to wildtype
629 peptide abundance. For nuclear IP of cell lines, MaxQuant outputs were analyzed using Differential
630 Expression of Proteins (DEP) package in R.
631
632 Chromatin Immunoprecipitation (ChIP)
633 Cells were crosslinked with 1% formaldehyde in the culture medium for 15 minutes at room
634 temperature, followed by quenching with 125 mM glycine for 5 minutes. Cells were pelleted and
635 washed. The pellet was resuspended in RIPA buffer with protease inhibitor cocktail (Roche),
636 incubated on ice, and sonicated to shear chromatin (~1 kb fragments). The lysate was centrifuged
637 at 12,000 x g for 10 minutes at 4 °C, and the volume was increased with dilution buffer (165 mM
638 NaCl, 0.01% SDS, 1.1% Triton X-100, 1.2 mM EDTA, 16.7 mM Tris–HCl, pH 8.0). Chromatin was
639 incubated with 5 µg of anti-RNAPII (Santa Cruz; F-12) for overnight at 4 °C. Chromatin-Antibody
640 mix was incubated with pre-washed Dynabeads and incubated at RT for 45 minutes. Beads were
641 washed 5x in dilution buffer and eluted in genomic DNA extraction kit (Macharey-Nagel) lysis
642 buffer, resuspended in 50 µL of water. PCR was performed using purified DNA and compared to
643 input samples. Two-sided Student's t-tests were carried out to calculate *P* value.

644 Nuclear localization calculation
645 Nuclear localization was calculated as a ratio of the immunofluorescent co-localization signal of
646 anti-HA with nuclear regions compared to anti-HA signal with cytoplasmic regions, determined as
647 cellular regions lacking in DAPI signal. The same calculation was performed for 28S rRNA. All
648 calculations were carried out with ImageJ. Cytoplasmic/Nuclear signal ratios for each cell were

649 compiled and underwent one-way ANOVA with Dunnett correction for multiple comparisons
650 across conditions.
651
652 Tissue RNA-seq
653 Explanted frozen patient heart tissue was homogenized using pestle and mortar under liquid
654 nitrogen. Homogenized tissue was submerged in TRIzol and extracted using Direct-zol kit (Zymo
655 Research). RNA integrity was analyzed with Bioanalyzer electrophoresis. Samples underwent
656 poly(A) RNA pulldown and libraries were constructed using Illumina TruSeq chemistry. Libraries
657 were sequenced at Columbia Sulzberger Genome Center with NovaSeq 6000 (Illumina). RTA
658 (Illumina) was used for base calling and bcl2fastq2 (version 2.19) for converting BCL to fastq format.
659 Gene expression was quantified using kallisto with a customized transcriptome index (human
660 MANE select). RNA-seq data for three age-matched control samples were downloaded from
661 European Nucleotide Archive (ENA project PRJEB26969, sample ID: 5818sTS, 5828sTS, and
662 5836sTS) and analyzed similarly. DESeq2 was used for differential gene expression analysis.
663
664
665 References

666 1. Van Raay, T.J., Connors, T.D., Klinger, K.W., Landes, G.M. & Burn, T.C. A novel ribosomal
667 protein L3-like gene (RPL3L) maps to the autosomal dominant polycystic kidney disease
668 gene region. Genomics 37, 172-176 (1996).
669 2. Chaillou, T., Zhang, X. & McCarthy, J.J. Expression of Muscle-Specific Ribosomal Protein L3-
670 Like Impairs Myotube Growth. J Cell Physiol 231, 1894-1902 (2016).
671 3. Shiraishi, C. et al. RPL3L-containing ribosomes determine translation elongation dynamics
672 required for cardiac function. Nat Commun 14, 2131 (2023).
673 4. Ganapathi, M. et al. Bi-allelic missense disease-causing variants in RPL3L associate neonatal
674 dilated cardiomyopathy with muscle-specific ribosome biogenesis. Hum Genet 139, 1443-
675 1454 (2020).
676 5. Das, B.B., Gajula, V., Arya, S. & Taylor, M.B. Compound Heterozygous Missense Variants in
677 RPL3L Genes Associated with Severe Forms of Dilated Cardiomyopathy: A Case Report and
678 Literature Review. Children (Basel) 9 (2022).
679 6. Nannapaneni, H. et al. Further Evidence of Autosomal Recessive Inheritance of RPL3L
680 Pathogenic Variants with Rapidly Progressive Neonatal Dilated Cardiomyopathy. J
681 Cardiovasc Dev Dis 9 (2022).
682 7. Al-Hassnan, Z.N. et al. Categorized Genetic Analysis in Childhood-Onset Cardiomyopathy.
683 Circ Genom Precis Med 13, 504-514 (2020).
684 8. Bajpai, A.K. et al. Exploring the Regulation and Function of Rpl3l in the Development of
685 Early-Onset Dilated Cardiomyopathy and Congestive Heart Failure Using Systems Genetics
686 Approach. Genes (Basel) 15 (2023).
687 9. Yang, Q. et al. Novel compound heterozygous variants in the RPL3L gene causing dilated
688 cardiomyopathy type-2D: a case report and literature review. BMC Med Genomics 16, 127
689 (2023).

690 10. Meskauskas, A., Harger, J.W., Jacobs, K.L. & Dinman, J.D. Decreased peptidyltransferase
691 activity correlates with increased programmed -1 ribosomal frameshifting and viral
692 maintenance defects in the yeast Saccharomyces cerevisiae. RNA 9, 982-992 (2003).
693 11. Milenkovic, I. et al. Dynamic interplay between RPL3- and RPL3L-containing ribosomes
694 modulates mitochondrial activity in the mammalian heart. Nucleic Acids Res 51, 5301-5324
695 (2023).
696 12. Grimes, K.M. et al. Rpl3l gene deletion in mice reduces heart weight over time. Frontiers
697 in Physiology 14 (2023).
698 13. Brown, L.P. & McCarthy, J.J., Vol. PhD (University of Kentucky, 2021).
699 14. Pillet, B. et al. Dedicated chaperones coordinate co-translational regulation of ribosomal
700 protein production with ribosome assembly to preserve proteostasis. Elife 11 (2022).
701 15. Iouk, T.L., Aitchison, J.D., Maguire, S. & Wozniak, R.W. Rrb1p, a yeast nuclear WD-repeat
702 protein involved in the regulation of ribosome biosynthesis. Mol Cell Biol 21, 1260-1271
703 (2001).
704 16. Schaper, S. et al. A yeast homolog of chromatin assembly factor 1 is involved in early
705 ribosome assembly. Curr Biol 11, 1885-1890 (2001).
706 17. Bergmann, O. et al. Dynamics of Cell Generation and Turnover in the Human Heart. Cell
707 161, 1566-1575 (2015).
708 18. Gay, D.M., Lund, A.H. & Jansson, M.D. Translational control through ribosome
709 heterogeneity and functional specialization. Trends Biochem Sci 47, 66-81 (2022).
710 19. Genuth, N.R. et al. A stem cell roadmap of ribosome heterogeneity reveals a function for
711 RPL10A in mesoderm production. Nat Commun 13, 5491 (2022).
712 20. Genuth, N.R. & Barna, M. The Discovery of Ribosome Heterogeneity and Its Implications
713 for Gene Regulation and Organismal Life. Mol Cell 71, 364-374 (2018).
714 21. Simsek, D. et al. The Mammalian Ribo-interactome Reveals Ribosome Functional Diversity
715 and Heterogeneity. Cell 169, 1051-1065 e1018 (2017).
716 22. Shi, Z. et al. Heterogeneous Ribosomes Preferentially Translate Distinct Subpools of mRNAs
717 Genome-wide. Mol Cell 67, 71-83 e77 (2017).
718 23. Li, H. et al. A male germ-cell-specific ribosome controls male fertility. Nature 612, 725-731
719 (2022).
720 24. Zou, Q. et al. Proteostasis regulated by testis-specific ribosomal protein RPL39L maintains
721 mouse spermatogenesis. iScience 24, 103396 (2021).
722 25. Meskauskas, A. & Dinman, J.D. Ribosomal protein L3: gatekeeper to the A site. Mol Cell 25,
723 877-888 (2007).
724 26. Burn, T.C. et al. Generation of a transcriptional map for a 700-kb region surrounding the
725 polycystic kidney disease type 1 (PKD1) and tuberous sclerosis type 2 (TSC2) disease genes
726 on human chromosome 16p3.3. Genome Res 6, 525-537 (1996).
727 27. Litvinukova, M. et al. Cells of the adult human heart. Nature 588, 466-472 (2020).
728 28. Consortium, G.T. The GTEx Consortium atlas of genetic regulatory effects across human
729 tissues. Science 369, 1318-1330 (2020).
730 29. Milenkovic, I. et al. RPL3L-containing ribosomes modulate mitochondrial activity in the
731 mammalian heart. bioRxiv, 2021.2012.2004.471171 (2021).
732 30. McNally, E.M. & Mestroni, L. Dilated Cardiomyopathy: Genetic Determinants and
733 Mechanisms. Circ Res 121, 731-748 (2017).

734 31. Rosenbaum, A.N., Agre, K.E. & Pereira, N.L. Genetics of dilated cardiomyopathy: practical
735 implications for heart failure management. Nat Rev Cardiol 17, 286-297 (2020).
736 32. Kamisago, M. et al. Mutations in sarcomere protein genes as a cause of dilated
737 cardiomyopathy. N Engl J Med 343, 1688-1696 (2000).
738 33. Di Fede, G. et al. A recessive mutation in the APP gene with dominant-negative effect on
739 amyloidogenesis. Science 323, 1473-1477 (2009).
740 34. Lee, T.M. et al. Pediatric Cardiomyopathies. Circ Res 121, 855-873 (2017).
741 35. Towbin, J.A. et al. Incidence, causes, and outcomes of dilated cardiomyopathy in children.
742 JAMA 296, 1867-1876 (2006).
743 36. Thorolfsdottir, R.B. et al. Coding variants in RPL3L and MYZAP increase risk of atrial
744 fibrillation. Commun Biol 1, 68 (2018).
745 37. Cheng, J. et al. Accurate proteome-wide missense variant effect prediction with
746 AlphaMissense. Science 381, eadg7492 (2023).
747 38. Jumper, J. et al. Highly accurate protein structure prediction with AlphaFold. Nature 596,
748 583-589 (2021).
749 39. Chen, S. et al. A genomic mutational constraint map using variation in 76,156 human
750 genomes. Nature 625, 92-100 (2024).
751 40. Bick, A.G. et al. Genomic data in the All of Us Research Program. Nature 627, 340-346
752 (2024).
753 41. Bycroft, C. et al. The UK Biobank resource with deep phenotyping and genomic data.
754 Nature 562, 203-209 (2018).
755 42. Sun, K.Y. et al. A deep catalogue of protein-coding variation in 983,578 individuals. Nature
756 631, 583-592 (2024).
757 43. Dorner, K., Ruggeri, C., Zemp, I. & Kutay, U. Ribosome biogenesis factors-from names to
758 functions. EMBO J 42, e112699 (2023).
759 44. Adamo, L., Rocha-Resende, C., Prabhu, S.D. & Mann, D.L. Reappraising the role of
760 inflammation in heart failure. Nat Rev Cardiol 17, 269-285 (2020).
761 45. Davidson, M.M. et al. Novel cell lines derived from adult human ventricular cardiomyocytes.
762 J Mol Cell Cardiol 39, 133-147 (2005).
763 46. Hedaya, O.M. et al. Secondary structures that regulate mRNA translation provide insights
764 for ASO-mediated modulation of cardiac hypertrophy. Nat Commun 14, 6166 (2023).
765 47. Guo, Y. & Pu, W.T. Cardiomyocyte Maturation: New Phase in Development. Circ Res 126,
766 1086-1106 (2020).
767 48. Thomas, D., Cunningham, N.J., Shenoy, S. & Wu, J.C. Human-induced pluripotent stem cells
768 in cardiovascular research: current approaches in cardiac differentiation, maturation
769 strategies, and scalable production. Cardiovasc Res 118, 20-36 (2022).
770 49. Bhutada, P. et al. Rbp95 binds to 25S rRNA helix H95 and cooperates with the Npa1
771 complex during early pre-60S particle maturation. Nucleic Acids Res 50, 10053-10077
772 (2022).
773 50. Sailer, C. et al. A comprehensive landscape of 60S ribosome biogenesis factors. Cell Rep 38,
774 110353 (2022).
775 51. Ismail, S. et al. Emergence of the primordial pre-60S from the 90S pre-ribosome. Cell Rep
776 39, 110640 (2022).

52. De Marchis, M.L., Giorgi, A., Schinina, M.E., Bozzoni, I. & Fatica, A. Rrp15p, a novel component of pre-ribosomal particles required for 60S ribosome subunit maturation. RNA 11, 495-502 (2005).
53. Tafforeau, L. et al. The complexity of human ribosome biogenesis revealed by systematic nucleolar screening of Pre-rRNA processing factors. Mol Cell 51, 539-551 (2013).
54. Bruning, L. et al. RNA helicases mediate structural transitions and compositional changes in pre-ribosomal complexes. Nat Commun 9, 5383 (2018).
55. Rodriguez-Mateos, M. et al. Role and dynamics of the ribosomal protein P0 and its related trans-acting factor Mrt4 during ribosome assembly in Saccharomyces cerevisiae. Nucleic Acids Res 37, 7519-7532 (2009).
56. Young, L.C. et al. Destabilizing NF1 variants act in a dominant negative manner through neurofibromin dimerization. Proc Natl Acad Sci U S A 120, e2208960120 (2023).
57. Utsumi, T. et al. Exclusive Characteristics of the p.E555K Dominant-Negative Variant in Autosomal Dominant E47 Deficiency. J Clin Immunol 44, 167 (2024).
58. Boettcher, S. et al. A dominant-negative effect drives selection of TP53 missense mutations in myeloid malignancies. Science 365, 599-604 (2019).
59. Gerasimavicius, L., Livesey, B.J. & Marsh, J.A. Loss-of-function, gain-of-function and dominant-negative mutations have profoundly different effects on protein structure. Nat Commun 13, 3895 (2022).
60. Dickerson, J.E. & Robertson, D.L. On the origins of Mendelian disease genes in man: the impact of gene duplication. Mol Biol Evol 29, 61-69 (2012).
61. El-Brolosy, M.A. et al. Genetic compensation triggered by mutant mRNA degradation. Nature 568, 193-197 (2019).
62. Rossi, A. et al. Genetic compensation induced by deleterious mutations but not gene knockdowns. Nature 524, 230-233 (2015).
63. El-Brolosy, M.A. & Stainier, D.Y.R. Genetic compensation: A phenomenon in search of mechanisms. PLoS Genet 13, e1006780 (2017).
64. van Heesch, S. et al. The Translational Landscape of the Human Heart. Cell 178, 242-260 e229 (2019).
65. Meier, F. et al. diaPASEF: parallel accumulation-serial fragmentation combined with data-independent acquisition. Nat Methods 17, 1229-1236 (2020).
66. Kulak, N.A., Pichler, G., Paron, I., Nagaraj, N. & Mann, M. Minimal, encapsulated proteomic-sample processing applied to copy-number estimation in eukaryotic cells. Nat Methods 11, 319-324 (2014).
67. Demichev, V., Messner, C.B., Vernardis, S.I., Lilley, K.S. & Ralser, M. DIA-NN: neural networks and interference correction enable deep proteome coverage in high throughput. Nat Methods 17, 41-44 (2020).

Figure legends

Figure 1. Hotspot variants G27D and D308N/V as potential drivers in *RPL3L*-linked DCM. a, Schematic representation of neonatal DCM-associated variants across the RPL3L protein. Each circle denotes a missense variant, while rectangles represent frameshift variants or the splice

819 variant (Δexon9). Variants are color-coded by family, with lines connecting compound
820 heterozygous variants identified in the same family. Variants identified in the three new cases are
821 highlighted with a star. The protein domains within RPL3L are labeled. The hotspot variants G27D
822 and D308N/V are emphasized in bold. **b**, Mapping of the variants (in red) onto the AlphaFold-
823 predicted 3D structure of RPL3L. The region encoded by exon 9, deleted in the splice variant
824 (Δexon9) is highlighted in salmon. Frameshift variants are not shown. **c**, Clustering of RPL3L
825 missense variants based on allele frequency (gnomAD) and predicted pathogenicity
826 (AlphaMissense). Variants identified in the same family are connected by dashed lines. **d**, Putative
827 human *RPL3L* KO in the general population. LOF: loss-of-function.
828
829 **Figure 2. Ribosome defects in explanted patient hearts**. **a**, Bioanalyzer electrophoresis of total
830 RNA isolated from explanted patient heart ventricular tissue and a control sample (human AC16
831 cells). **b**, Differential gene expression analysis comparing explanted heart tissue (N=2)and age-
832 matched healthy control heart ventricular tissue (N=3). Genes encoding 60S or 40S ribosomal
833 proteins are colored red or blue, respectively. *RPL3* and *RPL3L* are highlighted by yellow circles. **c**,
834 Cumulative distribution function plots for three significant gene signatures. Red indicates genes of
835 interest and black indicates all other genes. The median log2 fold change (log2fc) and Kolmogorov–
836 Smirnov test P values are also shown. **d**, RNA-seq read coverage (BAM file visualized in IGV genome
837 browser) showing that both D308N and T189M variants are equally expressed. **e**, Mass
838 spectrometry quantification of RPL3 (left), RPL3L (center), and total 60S proteins (right) relative
839 total 40S proteins in D308N/T189M patient ventricular tissue (N=2) and age-matched control
840 tissue (N=3). ** $P < 0.0001$. **f**, Intensity of the peptide containing the D308 residue in the T189M
841 variant and the peptide containing the N308 residue in the D308N variant normalized to the total
842 intensity in RPL3L. ns: not significant.

843 **Figure 3. Hotspot variants disrupt ribosome biogenesis and impairs cell viability**. **a**, Isogenic
844 AC16 human cardiomyocyte-like cell lines were generated to simultaneously knockdown (KD) RPL3
845 and overexpress HA-tagged RPL3L (or its variants) via a dox-inducible promoter. **b**, RPL3
846 knockdown after dox treatment. Total RNA was isolated from indicated cell lines and analyzed for
847 RPL3 levels. shScramble: cells expressing only a control scrambled shRNA. shRPL3: cells expressing
848 only the RPL3 targeting shRNA without RPL3L or its variants. RPL3L-WT/SNP/T189M/D308N: cells
849 with RPL3 KD and expresses either wild type or the indicated variant of RPL3L. **c**, Efficient
850 expression of RPL3L variants in AC16 cells after 120 hours Dox treatment. Total RNA isolated from
851 indicated cells was analyzed for RPL3L levels (N = 3 independent experiments). **d**, Bioanalyzer
852 electrophoresis on total RNA from indicated cell lines was quantified by ImageJ. **e**, Loss of
853 translation capacity in shRPL3 and D308N cells, but not control or T189M cells. RPL3+ (shScramble)
854 and RPL3L-expressing cells were separated by ultracentrifugation and fractionated in the presence
855 of cycloheximide (N = 3). **f**, Cell growth defects in D308N and shRPL3 cells. AC16-derived cells were
856 seeded at equal density and counted every 2 days (N = 4). The y-axis is shown on a logarithmic
857 scale. The percentage values represent the cell density at day 10 relative to the RPL3L-WT cell line.
858 **b ,c, f ,** Data are mean ± s.d. *: $P < 0.05$.
859
860 **Figure 4. Hotspot variants mislocalize and alter interactions with ribosome biogenesis factors**.
861 **a**, Cells were stained for anti-HA antibody (RPL3L and variants) and 28S rRNA FISH probes and

862 analyzed by 60x confocal microscopy. Scale bar = 50μm. **b**, Violin plot quantification of cytoplasmic
863 and nuclear abundances of HA (RPL3L) signals for indicated cell lines, measured per cell (N = 26-
864 41 cells). **c**, same as b but for 28S rRNA. One-way ANOVA was used for statistical analysis. **d**, PCA
865 analysis of the proteins co-immunoprecipitated with RPL3L variants. N=3. **e**, Enrichment of
866 GRWD1 and C7ORF50 in proteins co-immunoprecipitated with the hotspot variants D308N and
867 G27D compared to other variants. Peptide intensities are normalized by the median of all samples
868 and then log2-transformed. Error bars represent standard deviation. ns, not significant; ** P <
869 0.001; *** P < 0.0001; **** P < 0.00001.
870
871 **Figure 5. Non-hotspot variants drive post-transcriptional *RPL3* compensatory up-regulation**. **a**,
872 Compensatory increase of *RPL3* mRNA in R161W cells. DCM-associated *RPL3L* variants were
873 expressed for 120 hours in doxycycline and total RNA was extracted and analyzed for *RPL3* mRNA
874 levels (N = 3 independent experiments). **b**, Western blotting shows compensatory increase of RPL3
875 protein levels in R161W cells. Cells were treated as in (a) and whole-cell lysates were
876 immunoblotted with indicated antibodies (N = 3 independent experiments). **c**, No difference in
877 transcription activity in *RPL3* promoter assayed by ChIP-qPCR. Multiple primer pairs were used for
878 each region. An intergenic region upstream of *RPL3L* was used as a negative control of non-
879 transcribed region (N = 3). **d**, *RPL3* mRNA half-life is enhanced in R161W cells. *RPL3L*-expressing
880 variants were incubated with 50μg/ml RNA Polymerase II inhibitor α-amanitin for indicated
881 timepoints prior to analysis for *RPL3* mRNA relative to GAPDH, normalized to 0 hour (N = 3). **e**,
882 Compensatory *RPL3* mRNA increase occurs entirely in the cytoplasm in R161W cells. RNA
883 underwent subcellular fractionation for amplification of *RPL3* levels relative to GAPDH (N = 4).
884 **a,c,d,e**, Data are mean ± s.d. ns, not significant; * P < 0.01; *** P < 0.0001; **** P < 0.00001.
885
886 **Figure 6. Impaired protein synthesis in engineered compound heterozygous cells**. **a**, Cells stably
887 integrated with G27D, R161W, or both G27D and R161W were induced with dox for 144hrs.
888 Puromycin was added to 1uM final concentration for 30 minutes before cells were harvested for
889 Western blotting (N = 4). **b**, Quantification of puromycin incorporation. **c**, Quantification of RPL3
890 protein abundance. Data are mean ± s.d. ns, not significant; * P < 0.01.
891
892 **Extended Data Figure 1. iPSC cardiomyocytes (iPSC-CMs) do not express *RPL3L*.** Data was
893 analyzed from RNA-seq performed by Pozo et al (2022) comparing iPSC-CMs to fetal and adult
894 human heart.
895
896 **Extended Data Figure 2. The hotspot G27D variant mirrors the effects of D308N. a**, Cell growth
897 defect for G27D and R161W, as in **Fig. 3f**. **b**, Polysome fraction for G27D and R161W, as in **Fig. 3e**.
898 Data are mean ± s.d.
899
900 **Extended Data Figure 3. Enrichment of 60S ribosome biogenesis factors in proteins co-**
901 **immunoprecipitated with nuclear RPL3L variants.** Peptide intensities are normalized by the
902 median of all samples and then log2-transformed. Error bars represent standard deviation.
903

904 **Extended Data Figure 4. R161W does not incorporate into polysomes.** Monosome and
905 polysomal fractions from **Fig. 5** were isolated by TCA precipitation and immunoblotted for HA-tag.
906 Input (pre-ultracentrifugation) samples were loaded as controls.
907
908 **Extended Data Figure 5. No change in the expression of the *RPL3*-targeting shRNA in *RPL3L*-**
909 **expressing cells**. A custom annotation was used to detect shRNA hairpin from RNA-seq data
910 obtained from *RPL3L* variant-expressing cell lines. RPM, Reads per million (N = 3 biological
911 replicates). Error bars represent standard deviation. ns, not significant.
912
913 **Extended Data Figure 6. R161W does not induce higher *RPL3* intronic RNA as a proxy of**
914 **transcription levels**. Total RNA was isolated and cDNA was synthesized using random primers.
915 Primers targeting intron 3 and intron 9 of *RPL3* were used for amplification (N = 3). Error bars
916 represent standard deviation. ns, not significant.
917

Figure 1

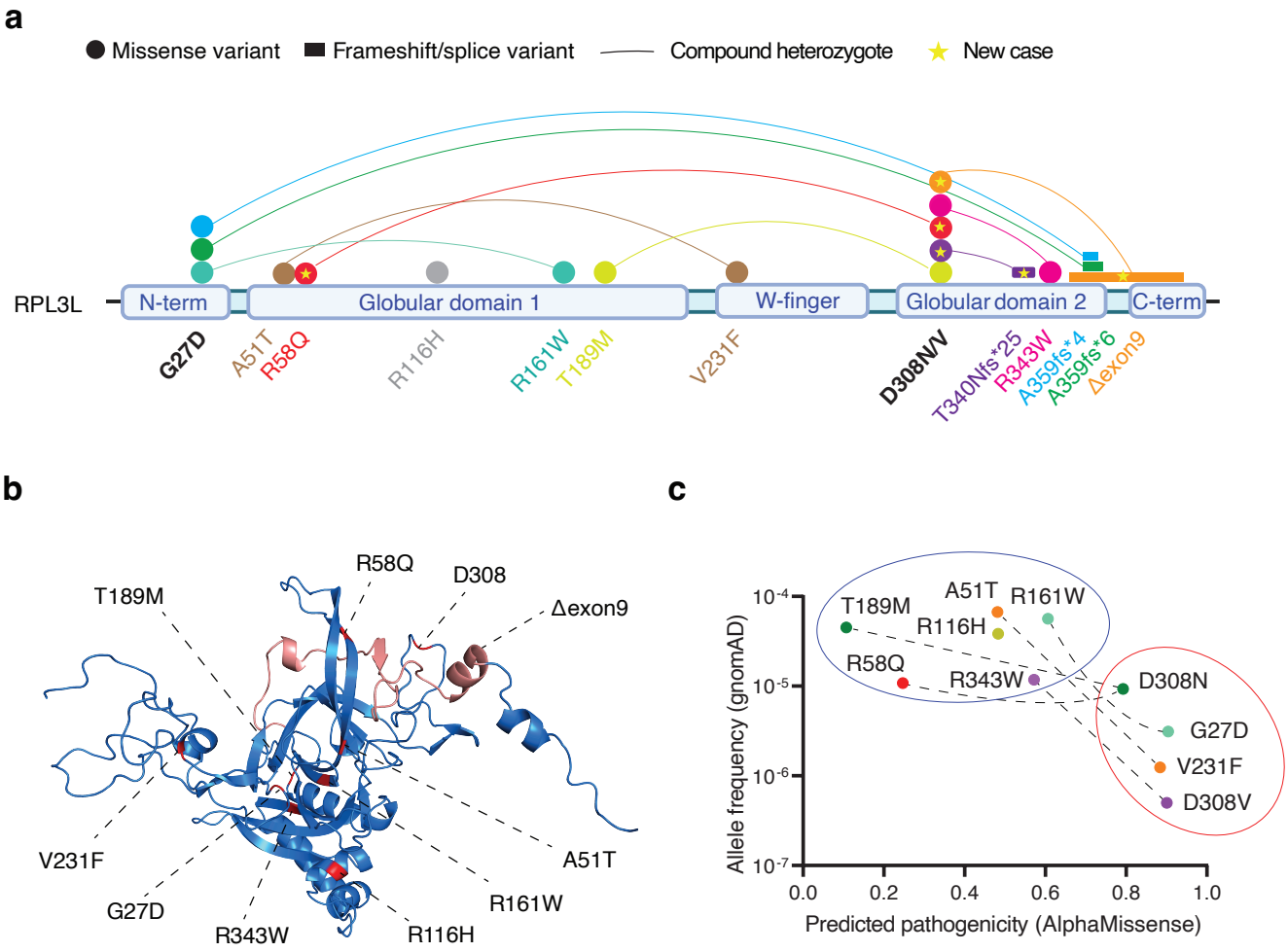

d

Putative LOF variant	Allele frequency	Homozygous humans
R226X (stop-gain)	1.67×10^{-5}	1 (gnomAD)
c.1167+1G>A (splice donor) (Δexon9)	2.49×10^{-3}	9 (gnomAD)
	1.70×10^{-3}	2 (AllofUs)
	3.41×10^{-3}	6 (UK Biobank)

Figure 1. Hotspot variants G27D and D308N/V as potential drivers in *RPL3L*-linked DCM. a, Schematic representation of neonatal DCM-associated variants across the RPL3L protein. Each circle denotes a missense variant, while rectangles represent frameshift variants or the splice variant (Δexon9). Variants are color-coded by family, with lines connecting compound heterozygous variants identified in the same family. Variants identified in the three new cases are highlighted with a star. The protein domains within RPL3L are labeled. The hotspot variants G27D and D308N/V are emphasized in bold. **b**, Mapping of the variants (in red) onto the AlphaFold-predicted 3D structure of RPL3L. The region encoded by exon 9, deleted in the splice variant (Δexon9) is highlighted in salmon. Frameshift variants are not shown. **c**, Clustering of RPL3L missense variants based on allele frequency (gnomAD) and predicted pathogenicity (AlphaMissense). Variants identified in the same family are connected by dashed lines. **d**, Putative human *RPL3L* KO in the general population. LOF: loss-of-function.

Figure 2

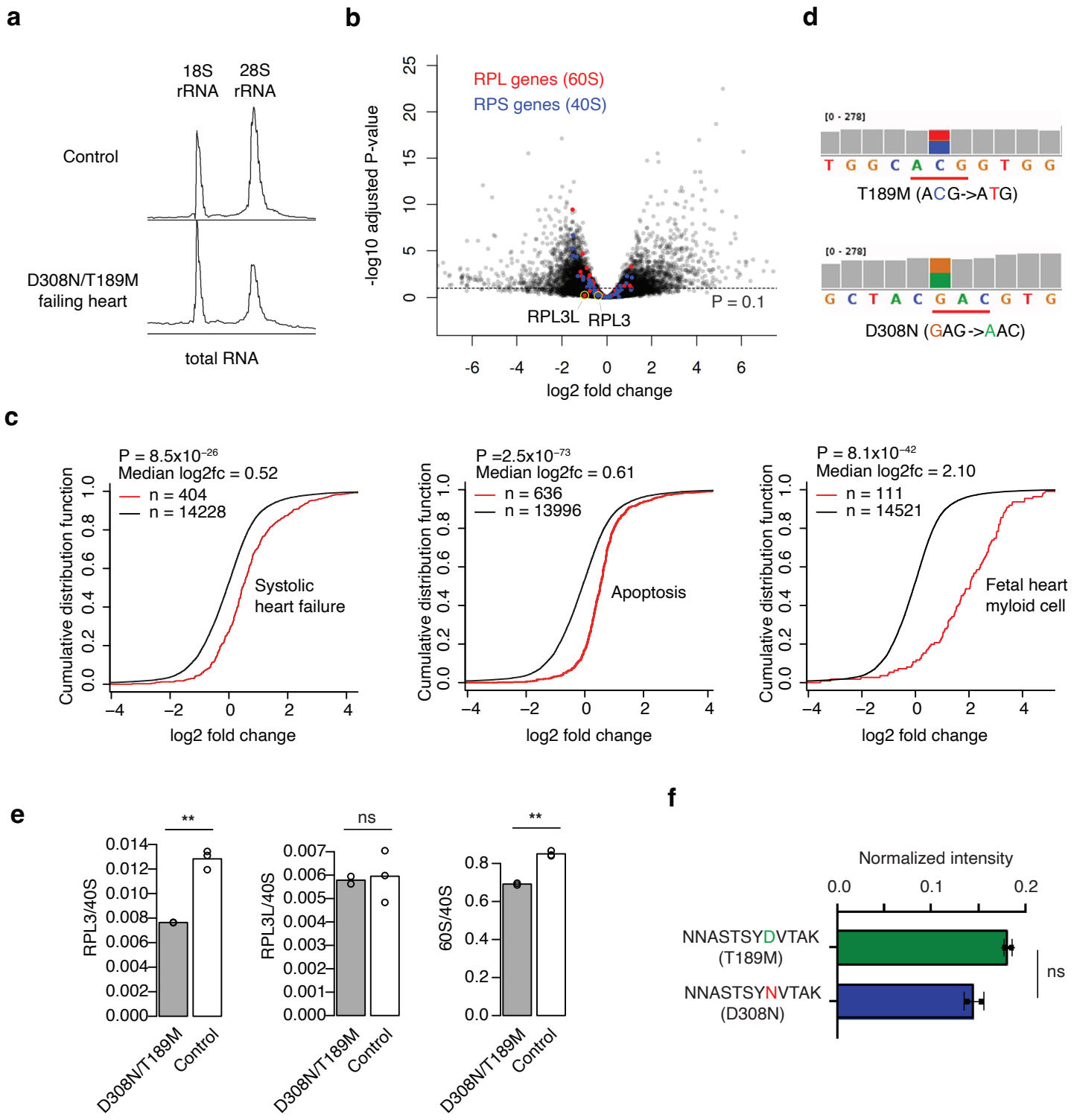

Figure 2. Ribosome defects in explanted patient hearts. **a**, Bioanalyzer electrophoresis of total RNA isolated from explanted patient heart ventricular tissue and a control sample (human AC16 cells). **b**, Differential gene expression analysis comparing explanted heart tissue (N=2)and age-matched healthy control heart ventricular tissue (N=3). Genes encoding 60S or 40S ribosomal proteins are colored red or blue, respectively. *RPL3* and *RPL3L* are highlighted by yellow circles. **c**, Cumulative distribution function plots for three significant gene signatures. Red indicates genes of interest and black indicates all other genes. The median log2 fold change (log2fc) and Kolmogorov–Smirnov test P values are also shown. **d**, RNA-seq read coverage (BAM file visualized in IGV genome browser) showing that both D308N and T189M alleles are equally expressed. **e**, Mass spectrometry quantification of RPL3 (left), RPL3L (center), and total 60S proteins (right) relative total 40S proteins in D308N/T189M patient ventricular tissue (N=2) and age-matched control tissue (N=3). ** $P < 0.0001$. **f**, Intensity of the peptide containing the D308 residue in the T189M variant and the peptide containing the N308 residue in the D308N variant normalized to the total intensity in RPL3L. ns: not significant.

Figure 3

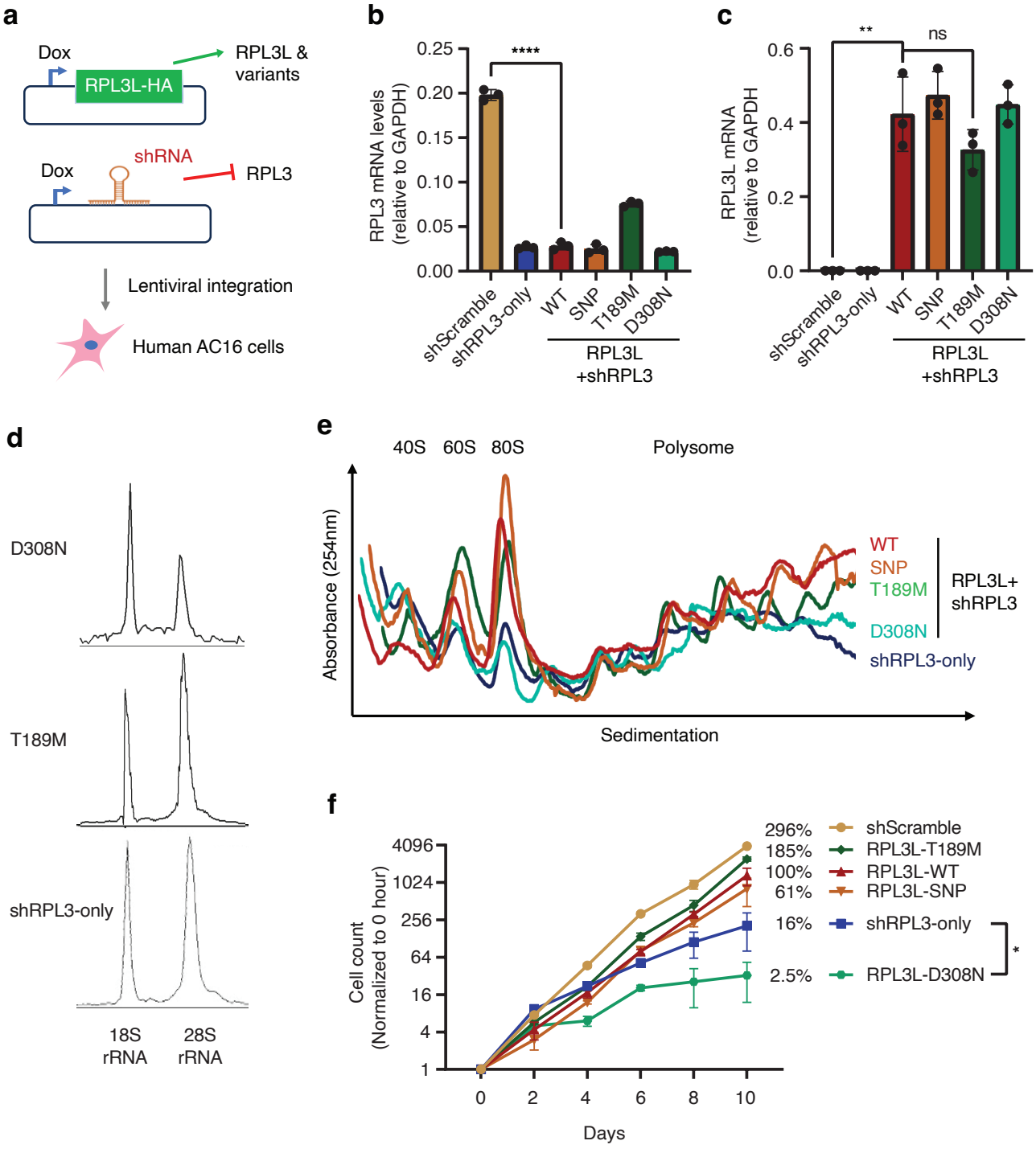

Figure 3. Hotspot variants disrupt ribosome biogenesis and impairs cell viability. **a**, Isogenic AC16 human cardiomyocyte-like cell lines were generated to simultaneously knockdown (KD) RPL3 and overexpress HA-tagged RPL3L (or its variants) via a dox-inducible promoter. **b**, RPL3 knockdown after dox treatment. Total RNA was isolated from indicated cell lines and analyzed for RPL3 levels. shScramble: cells expressing only a control scrambled shRNA. shRPL3: cells expressing only the RPL3 targeting shRNA without RPL3L or its variants. RPL3L-WT/SNP/T189M/D308N: cells with RPL3 KD and expresses either wild type or the indicated variant of RPL3L. **c**, Efficient expression of RPL3L variants in AC16 cells after 120 hours Dox treatment. Total RNA isolated from indicated cells was analyzed for RPL3L levels (N = 3 independent experiments). **d**, Bioanalyzer electrophoresis on total RNA from indicated cell lines was quantified by ImageJ. **e**, Loss of translation capacity in shRPL3 and D308N cells, but not control or T189M cells. RPL3+ (shScramble) and RPL3L-expressing cells were separated by ultracentrifugation and fractionated in the presence of cycloheximide (N = 3). **f**, Cell growth defects in D308N and shRPL3 cells. AC16-derived cells were seeded at equal density and counted every 2 days (N = 4). The y-axis is shown on a logarithmic scale. The percentage values represent the cell density at day 10 relative to the RPL3L-WT cell line. **b ,c, f ,** Data are mean ± s.d. *: $P < 0.05$.

Figure 4

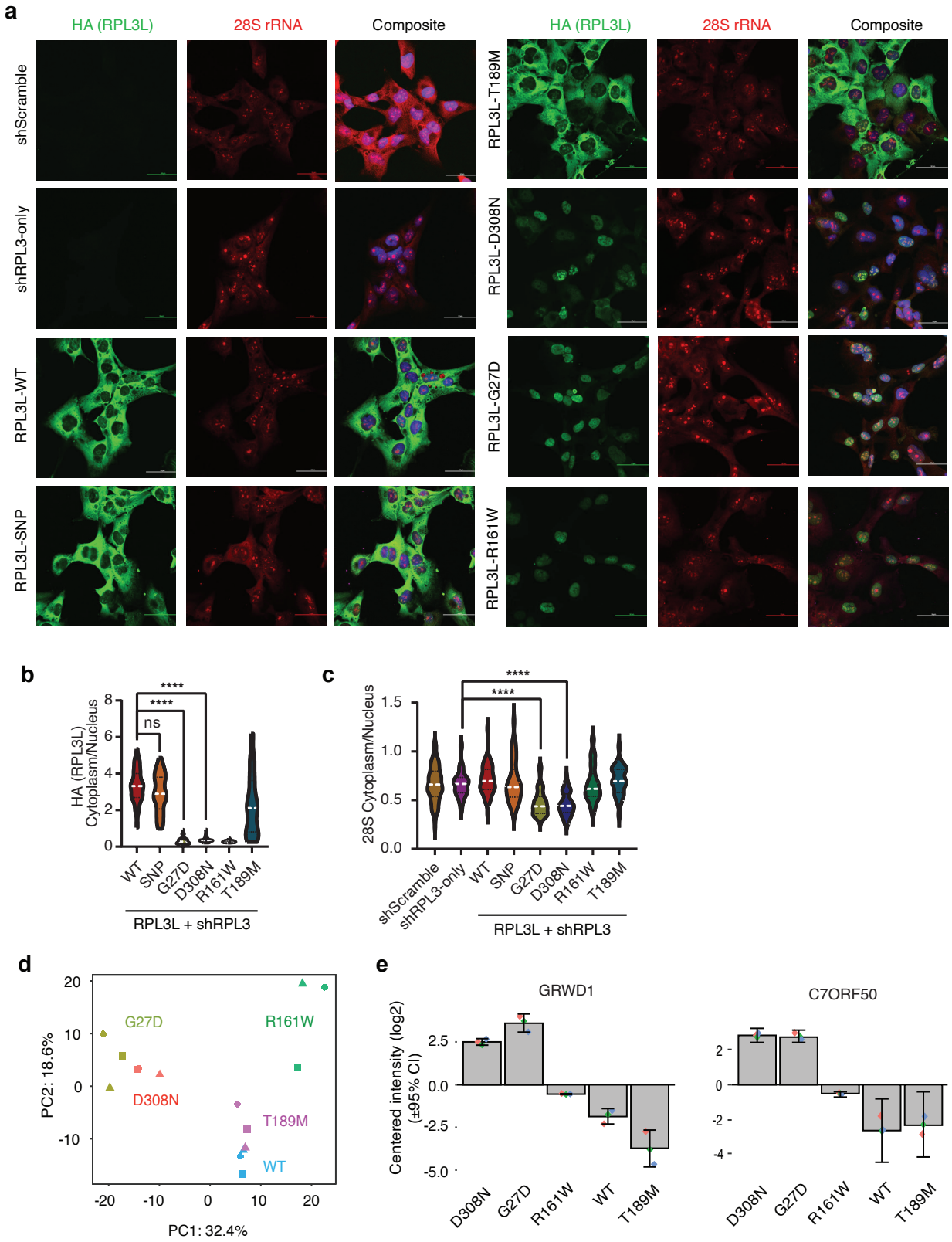

Figure 4. Hotspot variants mislocalize and alter interactions with ribosome biogenesis factors. **a**, Cells were stained for anti-HA antibody (RPL3L and variants) and 28S rRNA FISH probes and analyzed by 60x confocal microscopy. Scale bar = 50µm. **b**, Violin plot quantification of cytoplasmic and nuclear abundances of HA (RPL3L) signals for indicated cell lines, measured per cell (N = 26-41 cells). **c**, same as b but for 28S rRNA. One-way ANOVA was used for statistical analysis. **d**, PCA analysis of the proteins co-immunoprecipitated with RPL3L variants. N=3. **e**, Enrichment of GRWD1 and C7ORF50 in proteins co-immunoprecipitated with the hotspot variants D308N and G27D compared to other variants. Peptide intensities are normalized by the median of all samples and then log2-transformed. Error bars represent standard deviation. ns, not significant; ** $P < 0.001$; *** $P < 0.0001$; **** $P < 0.00001$.

Figure 5

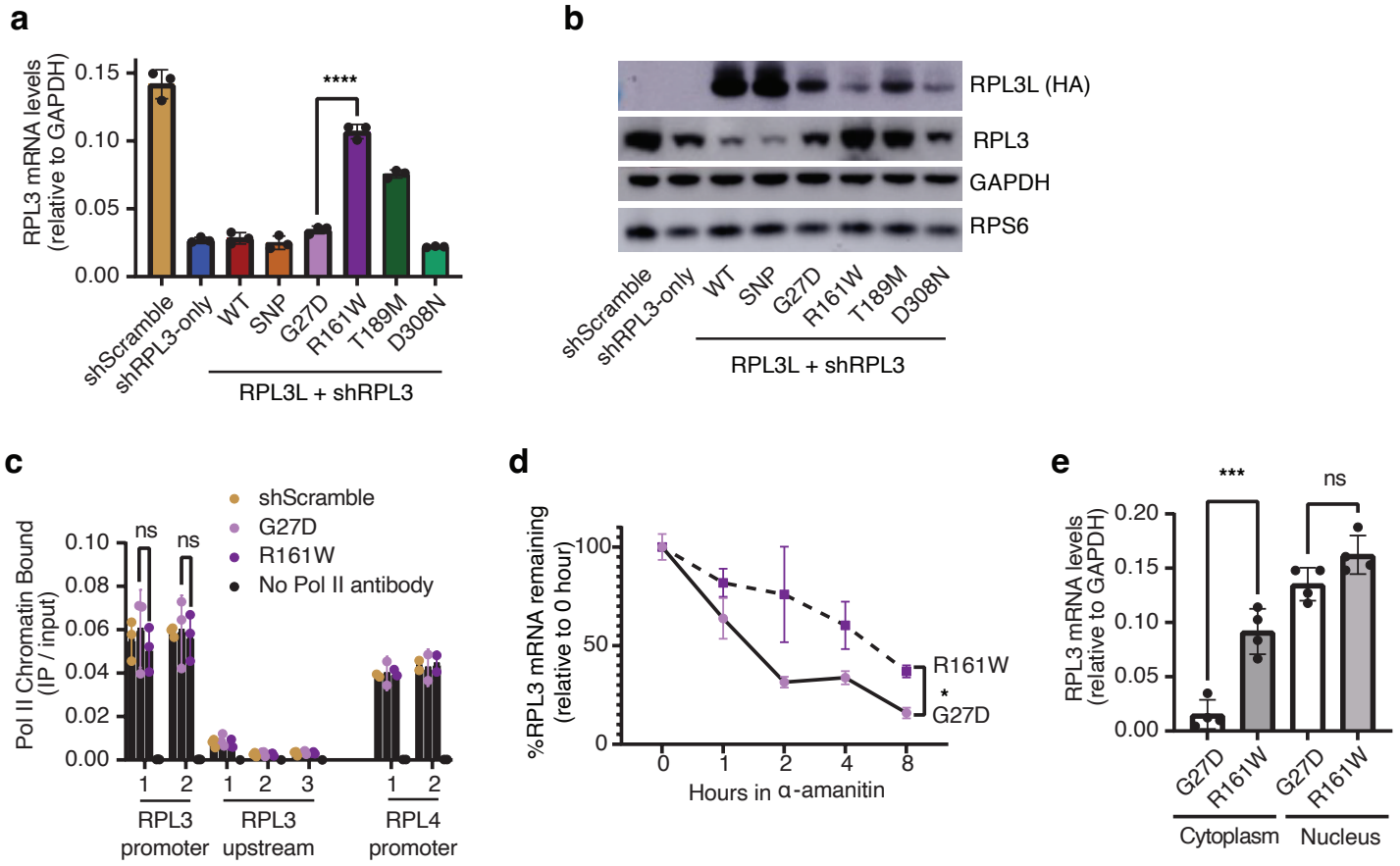

Figure 5. Non-hotspot variants drive post-transcriptional *RPL3* compensatory up-regulation. **a**, Compensatory increase of *RPL3* mRNA in R161W cells. DCM-associated *RPL3L* variants were expressed for 120 hours in doxycycline and total RNA was extracted and analyzed for *RPL3* mRNA levels (N = 3 independent experiments). **b**, Western blotting shows compensatory increase of RPL3 protein levels in R161W cells. Cells were treated as in (a) and whole-cell lysates were immunoblotted with indicated antibodies (N = 3 independent experiments). **c**, No difference in transcription activity in *RPL3* promoter assayed by ChIP-qPCR. Multiple primer pairs were used for each region. An intergenic region upstream of *RPL3L* was used as a negative control of non-transcribed region (N = 3). **d**, *RPL3* mRNA half-life is enhanced in R161W cells. *RPL3L*-expressing variants were incubated with 50μg/ml RNA Polymerase II inhibitor α-amanitin for indicated timepoints prior to analysis for *RPL3* mRNA relative to GAPDH, normalized to 0 hour (N = 3). **e**, Compensatory *RPL3* mRNA increase occurs entirely in the cytoplasm in R161W cells. RNA underwent subcellular fractionation for amplification of *RPL3* levels relative to GAPDH (N = 4). **a,c,d,e**, Data are mean ± s.d. ns, not significant; * $P < 0.01$; *** $P < 0.0001$; **** $P < 0.00001$.

Figure 6

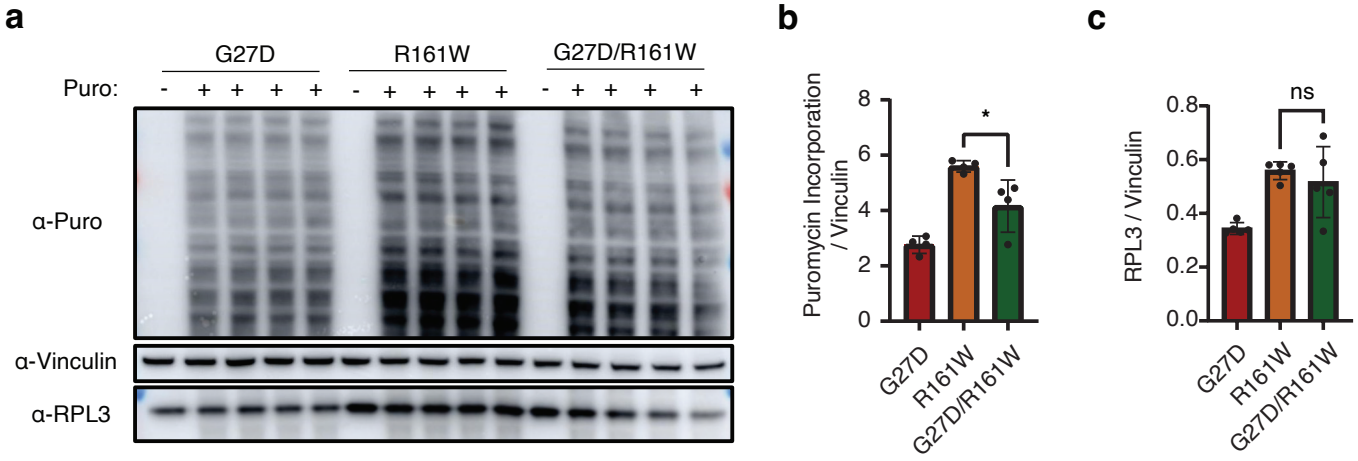

Figure 6. Impaired protein synthesis in engineered compound heterozygous cells. **a**, Cells stably integrated with G27D, R161W, or both G27D and R161W were induced with dox for 144hrs. Puromycin was added to 1uM final concentration for 30 minutes before cells were harvested for Western blotting (N = 4). **b**, Quantification of puromycin incorporation. **c**, Quantification of RPL3 protein abundance. Data are mean ± s.d. ns, not significant; * $P < 0.01$.

Extended Data Figure 1

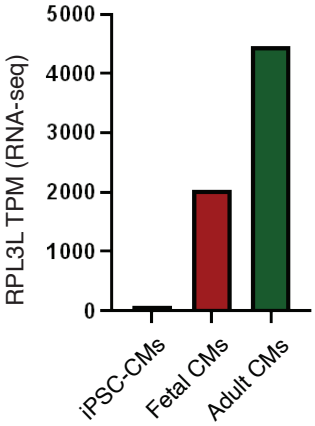

Extended Data Figure 1. iPSC cardiomyocytes (iPSC-CMs) do not express *RPL3L*. Data was analyzed from RNA-seq performed by Pozo et al (2022) comparing iPSC-CMs to fetal and adult human heart.

Extended Data Figure 2

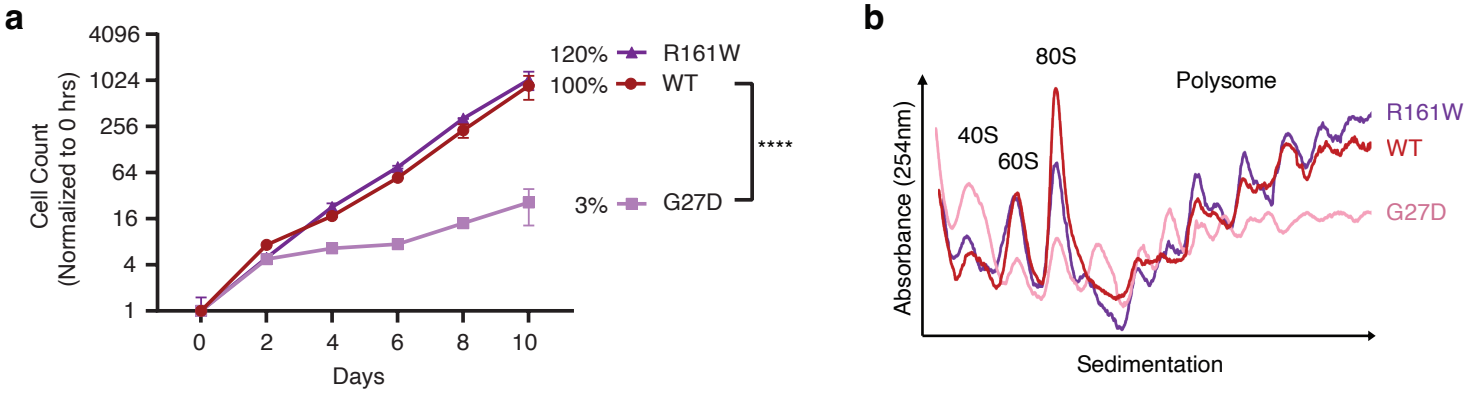

Extended Data Figure 2. The hotspot G27D variant mirrors the effects of D308N. a, Cell growth defect for G27D and R161W, as in **Fig. 3f**. **b**, Polysome fraction for G27D and R161W, as in **Fig. 3e**. Data are mean ± s.d.

Extended Data Figure 3

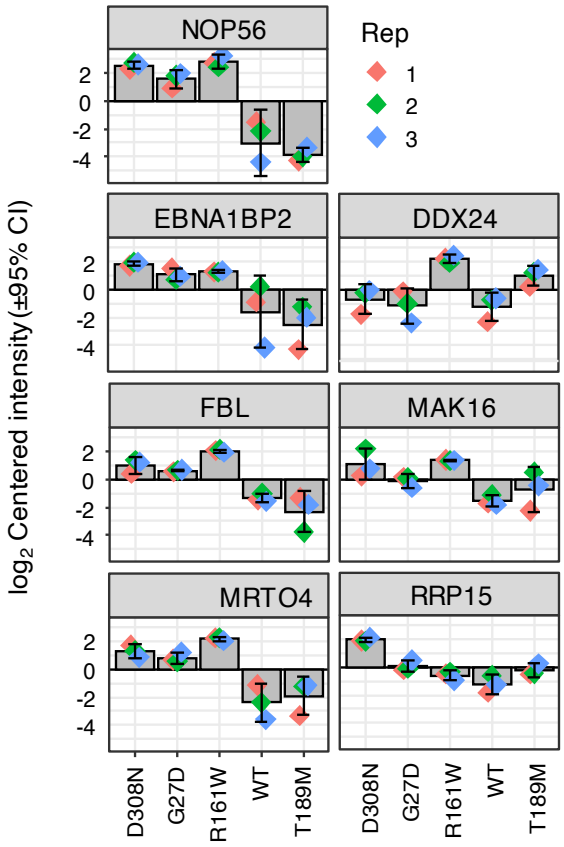

Extended Data Figure 3. Enrichment of 60S ribosome biogenesis factors in proteins co-immunoprecipitated with nuclear RPL3L variants. Peptide intensities are normalized by the median of all samples and then log2-transformed. Error bars represent standard deviation.

Extended Data Figure 4

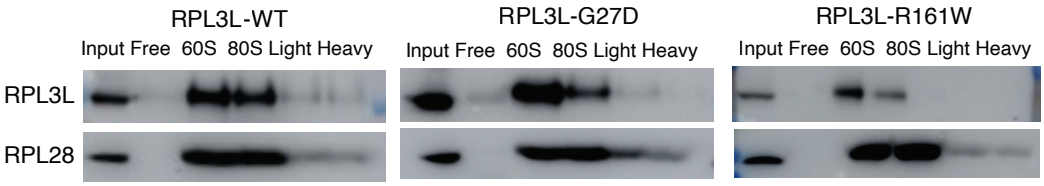

Extended Data Figure 4. R161W does not incorporate into polysomes. Monosome and polysomal fractions from **Fig. 5** were isolated by TCA precipitation and immunoblotted for HA-tag. Input (pre-ultracentrifugation) samples were loaded as controls.

Extended Data Figure 5

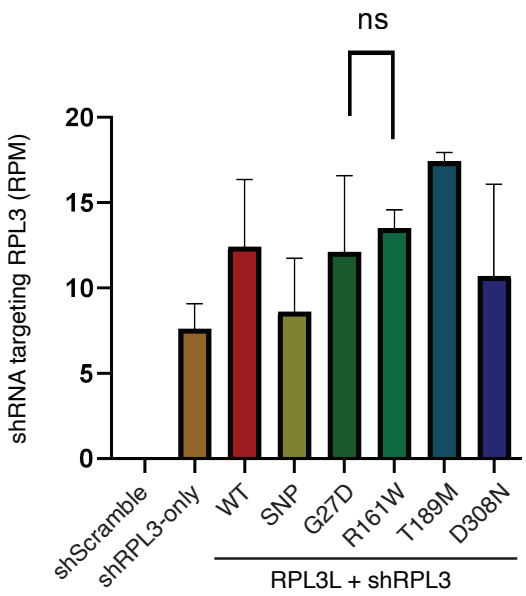

Extended Data Figure 5. No change in the expression of the *RPL3*-targeting shRNA in *RPL3L*-expressing cells. A custom annotation was used to detect shRNA hairpin from RNA-seq data obtained from *RPL3L* variant-expressing cell lines. RPM, Reads per million (N = 3 biological replicates). Error bars represent standard deviation. ns, not significant.

Extended Data Figure 6

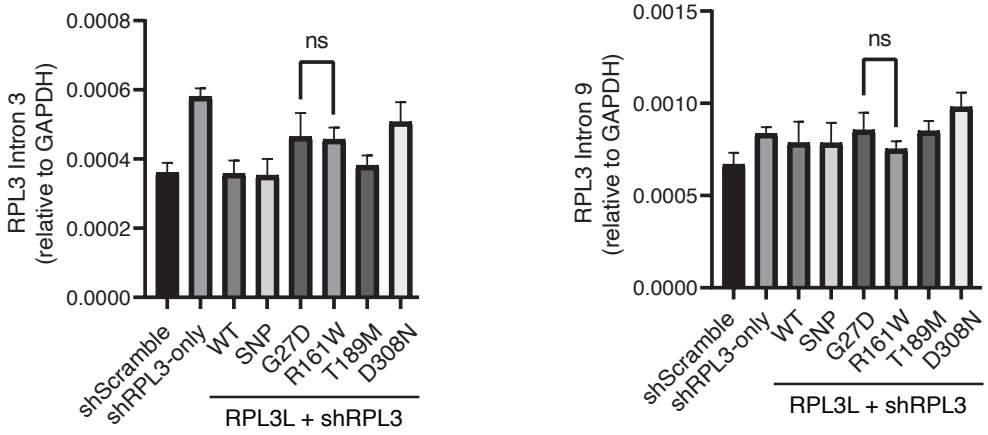

Extended Data Figure 6. R161W does not induce higher *RPL3* intronic RNA as a proxy of transcription levels. Total RNA was isolated and cDNA was synthesized using random primers. Primers targeting intron 3 and intron 9 of *RPL3* were used for amplification (N = 3). Error bars represent standard deviation. ns, not significant.